Improved absolute clock stability by the joint interrogation of two atomic ensembles

Weidong Li,[1,2] Shuyuan Wu,[3] Augusto Smerzi,[3,4] and Luca Pezzè[3,4]

[1]*Shenzhen Key Laboratory of Ultraintense Laser and Advanced Material Technology, Center for Advanced Material Diagnostic Technology, and College of Engineering Physics, Shenzhen Technology University, Shenzhen 518118, China*

[2]*Guangdong Provincial Key Laoratory of Quantum Science and Engineering, Southern University of Science and Technology, Shenzhen 518055, China*

[3]*QSTAR, INO-CNR and LENS, Largo Enrico Fermi 2, 50125 Firenze, Italy*

[4]*Institute of Theoretical Physics and Department of Physics, Shanxi University, Taiyuan 030006, China*

(Received 21 March 2022; accepted 31 March 2022; published 19 May 2022)

Improving the clock stability is of fundamental importance for the development of quantum-enhanced metrology. One of the main limitations arises from the randomly fluctuating local oscillator (LO) frequency, which introduces "phase slips" for long interrogation times and hence the failure of the frequency-feedback loop. Here we propose a strategy to improve the stability of atomic clocks by interrogating two atomic ensembles sharing the same LO. The two ensembles are prepared in coherent spin states pointing along orthogonal directions in the Bloch sphere. While standard Ramsey interrogation can only determine phases unambiguously in the interval $[-\pi/2, \pi/2]$, the joint interrogation allows for an extension to $[-\pi, \pi]$, resulting in a relaxed restriction of the Ramsey time and improvement of absolute clock stability. Theoretical predictions are supported by *ab initio* numerical simulation for white and correlated LO noise. While our basic protocol uses uncorrelated atoms, we further extended it to include spin-squeezing and further improving the scaling of clock stability with the number of atoms. Our protocol can be readily tested in current state-of-the-art experiments.

DOI: 10.1103/PhysRevA.105.053116

I. INTRODUCTION

The basic working principle of a passive atomic clock [1–5] is to stabilize the frequency of a local oscillator (LO) to an atomic resonance ω_0. Many atomic clock schemes are based on Ramsey interferometry [6]. In this case, the unavoidable frequency fluctuations of the LO accumulate during an interrogation time T and result in an overall rotation of the collective pseudospin of N two-level atoms by a stochastic angle θ. This angle is estimated by measuring the population imbalance of the two clock levels. The interferometer signal is a sinusoidal function of θ and can be inverted only in a restricted interval (also indicated as inversion region) where the function is monotonic. The phase estimate is then converted into a time-averaged frequency estimate that is used to steer the LO frequency toward ω_0. The frequency stability can be improved by increasing the interrogation time as long as θ remains within the inversion region. The stochastic occurrence of an accumulated phase shift outside the inversion region is generally indicated as a "phase slip" (or "fringe hop") and prevents the unbiased correction of the LO frequency. Within conventional phase-estimation methods, phase slips occur when $|\theta| \geqslant \pi/2$, see Fig. 1 and details below. In current atomic clocks, such as those exploiting ultrastable lasers [7–14], the LO decoherence dominates over the atomic decoherence and thus sets the crucial limitation to the stability.

Methods to avoid phase slips and thus extend the interrogation time have an immediate practical relevance and are thus attracting increasing interest in the literature [15–25]. Some proposals [16,17] considered the simultaneous use of multiple atomic ensembles characterized by different transition frequencies, which are phase-locked via a frequency comb. This method allows to extend the interrogation time of the ensemble characterized by the higher atomic transition frequency. In contrast, the authors of Refs. [16,18] considered ensembles having the same transition frequency but probed for different times. In this case, it is possible to extend the interrogation of the ensemble probed for the shorter time. However, both these methods do not allow to extend the interrogation time of the ensemble characterized by the smaller transition frequency or the ensemble probed for the longer time [16–18]. Another possibility is to phase-lock (via successive quantum nondemolition measurements) the LO to the atomic ensemble and thus increase the Ramsey interrogation time while avoiding phase slips [19–24].

In this paper, we propose a strategy to improve the frequency stability by interrogating simultaneously two atomic ensembles that share the same LO and the same atomic transition, see Fig. 1(a). The frequency-correction scheme is based on two Ramsey interferometers having the same interrogation time. The atomic ensembles are prepared in two coherent spin states that points to two orthogonal axes in the Bloch sphere. The two interferometers are thus characterized by Ramsey fringes that are dephased by an angle $\pi/2$, see Fig. 1(b). By combining the independent phase estimates obtained from the two interferometers, it is possible to extend the inversion region from $[-\pi/2, \pi/2]$ to $[-\pi, \pi]$: this increases the optimal Ramsey time and therefore also the absolute stability of the clock. Taking into account basic models of LO decoherence, we predict an improvement of the absolute stability by a factor of 4 (2) for the case of white (flicker) LO noise, when compared to the case of single-ensemble interrogation. Our

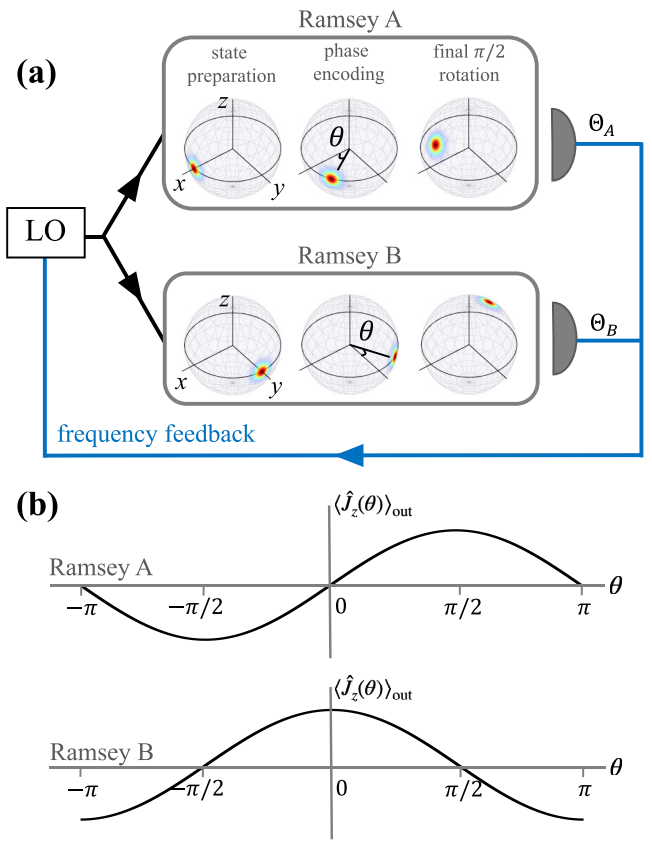

FIG. 1. (a) Scheme of the joint interrogation method. Two atomic ensembles are prepared in coherent spin states with mean spin direction pointing along orthogonal directions in the Bloch sphere (x axis for the Ramsey interferometer A and y axis for B) and interrogate the same LO. The accumulated phase θ is the same in both interferometers. The insets show Husimi distributions during the different interferometer operations. (b) Ramsey signal $\langle J_z(\theta)\rangle_{\rm out}$ as a function of θ for the two interferometers. Combining the two out-of-phase signals (see text) it is possible to obtain an unbiased estimate of θ in the full $[-\pi,\pi]$ interval.

protocol, differently from those of Refs. [19–21], does not require quantum nondemolition measurements and, differently from that of Refs. [16–18], it allows to extend the overall absolute stability. Our methods can be generalized to include spin-squeezed atomic ensembles to overcome the standard quantum limit.

The paper is organized as follows. In Sec. II, we introduce the Ramsey interferometer of Fig. 1 and discuss in detail its phase sensitivity. In Sec. III we review the basic concepts of atomic clocks. In particular, we focus on the detailed calculation of the optimal (Ramsey) interrogation time by carefully evaluating the bending point of the Allan variance. The optimal interrogation time defines the absolute (long-term) stability of the clock. Our methods to calculate the Allan variance avoid numerical instabilities that characterize the standard protocols in the presence of phase slips. Furthermore, in the case of white (correlated) LO noise, we provide analytical (semi-analytical) predictions that are found in excellent agreement with the results of *ab initio* Monte Carlo simulations. In Sec. IV, we analyze the impact of possible experimental imperfections in the preparation of coherent spin states, fluctuations of the atom number, and dead times. Finally, in Sec. V, we exploit the joint-Ramsey protocol in connection to a recent proposal of a hybrid quantum-classical clock using coherent- and squeezed-spin states [26].

II. RAMSEY INTERFEROMETRY AND PHASE SENSITIVITY

We consider N atoms, each modeled as a pseudospin-1/2 particle and introduce collective spin operators $\hat J_{x,y,z}=\sum_{j=1}^{N}\hat\sigma_{x,y,z}^{(j)}/2$, where $\hat\sigma_x=|\uparrow\rangle\langle\downarrow|+|\downarrow\rangle\langle\uparrow|$, $\hat\sigma_y=i(|\uparrow\rangle\langle\downarrow|-|\downarrow\rangle\langle\uparrow|)$, and $\hat\sigma_z=|\uparrow\rangle\langle\uparrow|-|\downarrow\rangle\langle\downarrow|$ are Pauli operators [27]. Initially, we prepare the N atoms in different superposition states of two eigenstates $|\uparrow\rangle$ and $|\downarrow\rangle$ of the atomic Hamiltonian (see discussion below). During the free evolution following the state preparation, the collective atomic pseudospin precesses around the z axis by an angle θ, which we specify later. The Ramsey sequence terminates with a $\pi/2$ rotation around the x axis. We assume that the duration of the $\pi/2$ pulse is short enough to neglect fluctuations of the LO leading to imperfections in the pulse rotation angle. In the noiseless case, the operations of both Ramsey interferometers of Fig. 1(a) are described by the unitary transformation $\hat U(\theta)=e^{-i\frac{\pi}{2}\hat J_x}e^{-i\theta\hat J_z}$. We have

$$\hat J_z(\theta)=\hat U^\dagger(\theta)\hat J_z\hat U(\theta)=\hat J_y\cos\theta+\hat J_x\sin\theta. \tag{1}$$

A measurement of $\hat J_z(\theta)$, corresponding to counting the relative number of particles between the two clock levels, provides an estimate of θ, depending on the interferometer scheme (single or joint, which we describe below).

A. Single-Ramsey interferometer

In the Ramsey interferometer A of Fig. 1(a), N_A atoms are prepared in the coherent-spin state [27,28]

$$|\psi_A\rangle=\left(\frac{|\uparrow\rangle+|\downarrow\rangle}{\sqrt{2}}\right)^{\otimes N_A}, \tag{2}$$

with mean spin direction pointing along the x axis $\langle\hat J_x\rangle_{\rm in}=\langle\psi_A|\hat J_x|\psi_A\rangle=N_A/2$. Using Eq. (1) and $\langle\hat J_y\rangle_{\rm in}=0$, the Ramsey signal is given by

$$\langle\hat J_z(\theta)\rangle_{\rm out}=\langle\psi_A|\hat J_z(\theta)|\psi_A\rangle=\frac{N_A}{2}\sin\theta. \tag{3}$$

Based on a single measurement of $\hat J_z$ with result $\mu_A=(N_\uparrow-N_\downarrow)/2$, where $N_\uparrow$ ($N_\downarrow$) is the number of particles in $|\uparrow\rangle$ ($|\downarrow\rangle$), we obtain the estimate

$$\Theta_A(\mu_A)=\arcsin\frac{2\mu_A}{N_A} \tag{4}$$

of θ. Notice that $\Theta_A(\mu_A)$ is a value in the inversion region $[-\pi/2,\pi/2]$ where Eq. (3) is monotonic, see Fig. 1(b).

The estimator Eq. (4) is a random variable with statistical mean value $\bar\Theta_A(\theta)=\mathcal{E}_{\mu_A|\theta}\{\Theta_A(\mu_A)\}$, where $\mathcal{E}_{\mu_A|\theta}\{\ldots\}=\sum_{\mu_A}P(\mu_A|\theta)\ldots$ indicates the statistical average over random measurement results obtained for a fixed value of θ, and $P(\mu_A|\theta)$ is the corresponding conditional probability to obtain the result μ_A. The fluctuations of the estimator are quantified by the variance $[\Delta\Theta_A(\theta)]^2=\mathcal{E}_{\mu_A|\theta}\{[\bar\Theta_A(\theta)-\Theta_A(\mu_A)]^2\}$ that

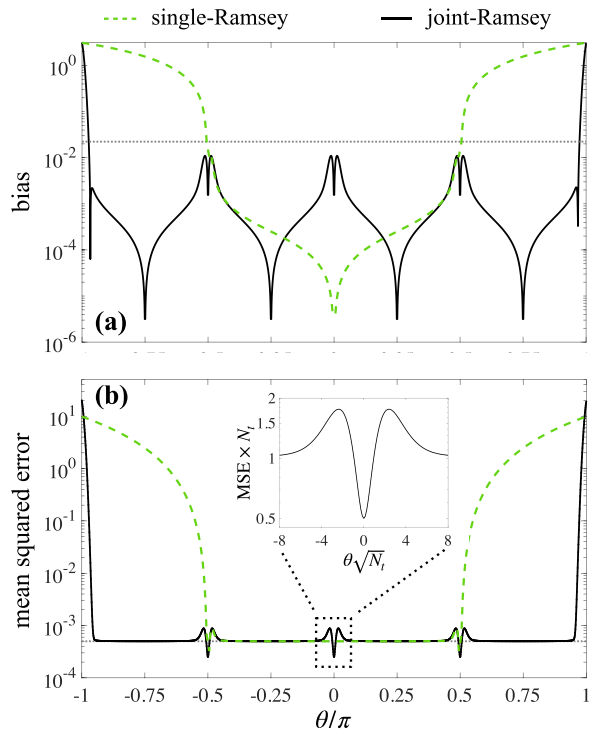

FIG. 2. (a) Estimator bias as a function of θ. The green dashed line is $|\theta - \bar{\Theta}_A(\theta)|$ for the single-Ramsey interferometer with Eq. (2) as input, while the black solid line is $|\theta - \bar{\Theta}_{AB}(\theta)|$ for the joint-Ramsey scheme. The horizontal dotted line is $1/\sqrt{N_t}$. (b) Mean squared error (MSE) as a function of θ. The green dashed (black solid) line is obtained for the single- (joint-) Ramsey interferometer. The horizontal dotted line is $1/N_t$. The inset is a zoom showing the mean squared error multiplied by N_t as a function of $\theta\sqrt{N_t}$ around $\theta = 0$. In both panels, the single and joint protocols are compared by fixing the total number of particles $N_t = 2000$, that is, $N_A = N_t$ for the single-Ramsey interferometer and $N_A = N_B = N_t/2$ for the joint-Ramsey scheme.

can be well approximated by the error propagation formula

$$[\Delta\Theta_A(\theta)]^2 \approx \frac{[\Delta\hat{J}_z(\theta)]^2_{\rm out}}{\left(d\langle\hat{J}_z(\theta)\rangle_{\rm out}/d\theta\right)^2} = \frac{1}{N_t}, \tag{5}$$

where $N_t = N_A$ is the total number of particles used in the interferometer. The right-hand side of the above equation is obtained using Eq. (1) and $[\Delta\hat{J}_z(\theta)]^2_{\rm out} = \langle\hat{J}_z^2\rangle_{\rm out} - \langle\hat{J}_z\rangle^2_{\rm out} = (N_A/4)\cos^2\theta$, which is due to $(\Delta\hat{J}_x)^2_{\rm in} = 0$, $\langle\hat{J}_x\hat{J}_z + \hat{J}_z\hat{J}_x\rangle_{\rm in} = 0$ and $(\Delta\hat{J}_z)^2_{\rm in} = N_A/4$, for the coherent state Eq. (2).

In Fig. 2(a) we show the estimator bias $|\theta - \bar{\Theta}_A(\theta)|$ (green dashed line). For $|\theta| \lesssim \pi/2$, we have $|\theta - \bar{\Theta}_A(\theta)| \ll \Delta\Theta_A(\theta)$. Instead, for $|\theta| \geqslant \pi/2$, outside the inversion region, the estimate (4) is characterized by a finite bias $|\theta - \bar{\Theta}_A(\theta)| \approx 2|\theta| - \pi$. In Fig. 2(b) we show the mean squared error of Θ_A,

$$\mathcal{E}_{\mu_A|\theta}\{[\Theta_A(\mu_A) - \theta]^2\} = [\Delta\Theta_A(\theta)]^2 + [\theta - \bar{\Theta}_A(\theta)]^2. \tag{6}$$

For $|\theta| \lesssim \pi/2$ we have $\mathcal{E}_{\mu_A|\theta}\{[\Theta_A(\mu_A) - \theta]^2\} \approx [\Delta\Theta_A(\theta)]^2 \approx 1/N_t$, as predicted by Eq. (5). In particular, $[\Delta\Theta_A(\theta)]^2$ does not depend on θ approximately in the full $[-\pi/2, \pi/2]$ interval. For $|\theta| \geqslant \pi/2$, the bias dominates and Eq. (6) is well approximated by $1/N_t + (2|\theta| - \pi)^2$.

B. Joint-Ramsey interferometer

The joint interferometer scheme is shown in Fig. 1(a). The first interferometer (indicated as Ramsey A) is a standard one, as discussed above. The second interferometer (Ramsey B) differs from the first one by the direction of the initial coherent spin state

$$|\psi_B\rangle = \left(\frac{|\uparrow\rangle + i|\downarrow\rangle}{\sqrt{2}}\right)^{\otimes N_B}, \tag{7}$$

which has a mean spin direction pointing along the y axis $\langle\hat{J}_y\rangle_{\rm in} = \langle\psi_B|\hat{J}_y|\psi_B\rangle = N_B/2$ and $\langle\hat{J}_x\rangle_{\rm in} = 0$. The Ramsey signal for the interferometer B is thus

$$\langle\hat{J}_z(\theta)\rangle_{\rm out} = \langle\psi_B|\hat{J}_z(\theta)|\psi_B\rangle = \frac{N_B}{2}\cos\theta, \tag{8}$$

with fluctuations $(\Delta\hat{J}_z(\theta))^2_{\rm out} = (N_B/4)\sin^2\theta$. A measurement of $\hat{J}_z$ with result μ_B, leads to an estimate

$$\Theta_B(\mu_B) = \arccos\frac{2\mu_B}{N_B}, \tag{9}$$

obtained by inverting Eq. (8). Notice that Eq. (8) is characterized by two inversion regions where the function of θ is monotonic: $[-\pi, 0]$ and $[0, \pi]$, see Fig. 1(b). Equation (8) is dephased by $\pi/2$ with respect to Eq. (3) due to the different initial state. The total number of particles used in the joint interferometer is $N_t = N_A + N_B$. In the following we will consider the case $N_A = N_B = N = N_t/2$. We will relax this assumption in Sec. IV.

The central idea of this work is to combine the two estimates $\Theta_A(\mu_A)$ and $\Theta_B(\mu_B)$ to obtain a joint estimate $\Theta_{AB}(\mu_A, \mu_B)$ of θ. Specifically, we define

$$\Theta_{AB}(\mu_A, \mu_B) = \begin{cases} \frac{\Theta_A(\mu_A)+\Theta_B(\mu_B)}{2} & \text{if } \mu_A > 0 \text{ and } \mu_B > 0, \\ \frac{\pi-\Theta_A(\mu_A)+\Theta_B(\mu_B)}{2} & \text{if } \mu_A > 0 \text{ and } \mu_B < 0, \\ \frac{\Theta_A(\mu_A)-\Theta_B(\mu_B)}{2} & \text{if } \mu_A < 0 \text{ and } \mu_B > 0, \\ \frac{-\pi-\Theta_A(\mu_A)-\Theta_B(\mu_B)}{2} & \text{if } \mu_A < 0 \text{ and } \mu_B > 0, \end{cases} \tag{10}$$

and, when the measurement results are $\mu_A = 0$ or $\mu_B = 0$,

$$\Theta_{AB}(\mu_A, \mu_B) = \begin{cases} 0 & \text{if } \mu_A = 0 \text{ and } \mu_B > 0, \\ \pi & \text{if } \mu_A = 0 \text{ and } \mu_B < 0, \\ \pi/2 & \text{if } \mu_A > 0 \text{ and } \mu_B = 0, \\ -\pi/2 & \text{if } \mu_A < 0 \text{ and } \mu_B = 0. \end{cases} \tag{11}$$

For instance, if $\mu_A \geqslant 0$ and $\mu_B \geqslant 0$, the true phase is most likely in the region $[0, \pi/2]$ where $\langle\hat{J}_z\rangle_{\rm out} \geqslant 0$ for both interferometers, see Fig. 1(b). In this case, the joint estimate $\Theta_{AB}(\mu_a, \mu_B)$ is thus simply chosen as the sum of Θ_A and Θ_B, divided by 2. Conversely, if $\mu_A \leqslant 0$ and $\mu_B \geqslant 0$, the true phase is most likely in the region $[-\pi/2, 0]$ where the Ramsey signal $\langle\hat{J}_z\rangle_{\rm out}$ is negative for the interferometer A and positive for the interferometer B, see Fig. 1(b). In this case, $\Theta_{AB}(\mu_a, \mu_B)$ is chosen as the difference between Θ_A and Θ_B divided by 2, and so on. This explains the choice of linear combination of Θ_A and Θ_B in Eq. (10).

In Fig. 2(a) we plot the bias $|\theta - \bar{\Theta}_{AB}(\theta)|$ as a function of θ, where $\bar{\Theta}_{AB}(\theta) = \mathcal{E}_{\mu_A,\mu_B|\theta}\{\Theta_{AB}(\mu_A, \mu_B)\}$ is the statistical mean value of the estimator (10), and $\mathcal{E}_{\mu_A,\mu_B|\theta}\{\ldots\} = \sum_{\mu_A,\mu_B} P(\mu_A|\theta)P(\mu_B|\theta)\ldots$ indicates statistical averaging over random independent measurement results μ_A and

μ_B. The bias is essentially negligible, $|\theta - \bar{\Theta}_{AB}(\theta)| \ll 1/\sqrt{N_t}$, in the full $\theta \in [-\pi, \pi]$ interval except around $\theta = 0, \pm\pi/2, \pm\pi$. For instance, for $0 \lesssim \theta \lesssim 1/\sqrt{N_A}$, one would expect to observe results $\mu_A \geqslant 0$ [since $\langle \hat{J}_z(\theta)\rangle_{\rm out} \geqslant 0$ for the interferometer A is positive for these values of θ, see Fig. 1(b)], but results $\mu_A < 0$ are also possible due to the finite width of the relative number of particles distribution $P(\mu_A|\theta)$. In this case, according to Eq. (10), we combine the two estimates according to $\Theta_{AB} = (\Theta_A - \Theta_B)/2$, thus introducing a bias approximately equal to 2θ. Similar considerations hold in regions of width $\approx 1/\sqrt{N_B}$ close to $\pm\pi/2$. Close to $\pm\pi$ the bias is much larger than around 0 and $\pm\pi/2$, see Fig. 2(a). Similarly as above, this bias is related to the finite width of the relative number of the particles' distribution. For instance, for $\pi - 1/\sqrt{N_A} \lesssim \theta \lesssim \pi$, it may happen that the measurement results give $\mu_A < 0$ and $\mu_B < 0$ (rather than the more likely $\mu_A > 0$ and $\mu_B < 0$). According to Eq. (10), this relative rare event leads to a large bias of approximately 2π. This qualitatively explains the increase of $|\theta - \bar{\Theta}_{AB}(\theta)|$ close to $\pm\pi$, as shown in Fig. 1(a).

In Fig. 2(b) we plot the mean square error around θ,

$$\mathcal{E}_{\mu_A,\mu_B|\theta}\{[\Theta_{AB}(\mu_a, \mu_B) - \theta]^2\} = [\Delta\Theta_{AB}(\theta)]^2 + [\theta - \bar{\Theta}_{AB}(\theta)]^2, \tag{12}$$

where $[\Delta\Theta_{AB}(\theta)]^2 = \mathcal{E}_{\mu_A,\mu_B|\theta}\{[\bar{\Theta}_{AB}(\theta) - \Theta_{AB}(\mu_A, \mu_B)]^2\}$ is the statistical variance of the joint estimator. Neglecting effects associated to the bias predicts

$$[\Delta\Theta_{AB}(\theta)]^2 = \frac{[\Delta\Theta_A(\theta)]^2 + [\Delta\Theta_B(\theta)]^2}{4} = \frac{1}{N_t}. \tag{13}$$

Equation (13) is numerically verified in the full $\theta \in [-\pi, \pi]$ interval except close to $0, \pm\pi/2, \pm\pi$ where the effect of the bias is not negligible. For instance, at $\theta = 0$, we find that $\langle \hat{J}_z\rangle_{\rm out} = N_B/2$ for the interferometer B, which implies $\mu_B = N_B/2$ and $\Theta_B(N_B/2) = 0$ [with vanishing statistical fluctuations since $(\Delta\hat{J}_z)^2_{\rm out} = 0$]. The estimator Θ_B is thus biased. Therefore, according to Eq. (10), $\Theta_{AB}(\mu_A, \mu_B) = \Theta_A(\mu_A)/2$, which implies $(\Delta\Theta_{AB})^2 = (\Delta\Theta_A)^2/2 = 1/(2N_t)$: the variance of the estimator Θ_{AB} drops by a factor of 2 with respect to Eq. (13) due to the bias of Θ_B. The behavior of $(\Delta\Theta_{AB})^2$ close to $\theta = 0$ is shown in the inset of Fig. 2(b). A similar behavior is observed close to $\theta = \pm\pi/2$, where $\langle \hat{J}_z\rangle_{\rm out} = \pm N/2$ for the interferometer A with vanishing fluctuations (due to the bias of Θ_A).

III. CLOCK OPERATIONS AND FIGURE OF MERIT

The clock operations are described by introducing three relevant quantities: (i) the atomic transition frequency ω_0 between two atomic levels; (ii) the free running (unlocked) LO frequency $\tilde{\omega}_{\rm LO}(t)$; and (iii) the stabilized LO frequency $\omega_{\rm LO}(t)$ obtained from periodic feedback corrections on the free-running LO.

The unlocked LO frequency $\tilde{\omega}_{\rm LO}(t)$ is affected by stochastic fluctuations that are characterized by a power spectral density $S(f) = h_{\rm LO}/f^\alpha$, with $\alpha = 0$ for white noise (also often indicated as frequency noise) and $\alpha = 1$ for flicker (or pink) noise, where $h_{\rm LO}$ is a prefactor. The accumulated phase during a time T is $\tilde{\theta}(T) = \int_T dt\ \delta\tilde{\omega}_{\rm LO}(t)$, where $\delta\tilde{\omega}_{\rm LO}(t) = \tilde{\omega}_{\rm LO}(t) - \omega_0$. The quantity $\tilde{\theta}(T)$ is a stochastic variable with a Gaussian statistical distribution of zero mean, $\mathcal{E}_{\tilde{\omega}}[\tilde{\theta}(T)] = 0$, and variance $v_\alpha(T)^2 = \mathcal{E}_{\tilde{\omega}}[\tilde{\theta}_{\rm LO}(T)^2]$, where $\mathcal{E}_{\tilde{\omega}}$ indicates statistical averaging over LO fluctuations. For white noise, we have $v_0(T)^2 = \gamma_{\rm LO}T$, where the dephasing rate is related to $h_{\rm LO}$ as $\gamma_{\rm LO}/\omega_0 = h_{\rm LO}\omega_{\rm LO}/2$. For flicker noise, we have $v_1(T)^2 = (\gamma_{\rm LO}T)^2$, where $\gamma_{\rm LO}/\omega_0 = \sqrt{h_{\rm LO} 2\chi \ln 2}$ and $\chi = 1.4$ is determined numerically (see Appendix for details on the numerical simulations of the LO signal).

To stabilize the LO frequency around ω_0, one first estimates the rotation angle that accumulates during the interrogation time T,

$$\theta(T) = \int_T dt\ \delta\omega_{\rm LO}(t), \tag{14}$$

where $\delta\omega_{\rm LO}(t) = \omega_{\rm LO}(t) - \omega_0$. From the estimated $\Theta(\mu)$, depending on the measurement result μ (for the joint Ramsey interferometer described in Sec. II B we identify $\mu \equiv \{\mu_A, \mu_B\}$), one obtains an estimate of the average LO frequency fluctuations, $\Theta(\mu)/T$ [29]. This value is subtracted from the signal $\delta\tilde{\omega}_{\rm LO}(t)$, resulting in a feedback loop. The estimation is repeated sequentially. In particular, during the nth Ramsey cycle, namely for $(n-1)T \leqslant t \leqslant nT$ (with $n = 2, \ldots, n_c$), the stabilized LO frequency is

$$\delta\omega_{\rm LO}(t) = \delta\tilde{\omega}_{\rm LO}(t) - \sum_{j=1}^{n-1} \frac{\Theta(\mu_j)}{T}, \tag{15}$$

where μ_j is the result of the jth measurement ($j = 1, \ldots, n-1$). Equation (15) provides the relation between the locked and the unlocked LO frequencies. We point out that, in the joint Ramsey scheme of Fig. 1(a), the two interferometers share the same LO (and thus see the same LO fluctuations) and are characterized by the same atomic transition, interrogation time, and number of particles, such that the phase shift $\theta(T)$ is common to both.

In the following, we evaluate the stability of the clock using the Allan variance, which is a common figure of merit. To compare the schemes based on single and joint Ramsey interferometry, it is crucial to evaluate accurately the optimal interrogation time. In particular, we introduce an expression for the calculation of the average Allan variance that avoids numerical instabilities due to phase slips and allows to obtain analytical (for white LO noise) or semi-analytical (for correlated LO noise) results. The clock schemes based on single and joint Ramsey interferometry are discussed in Secs. III B and III C, respectively. Notice that we neglect here the dead times between Ramsey interrogations (the impact of the dead times is discussed in Sec. IV C). We also assume that atomic decoherence occurs on timescales much longer than LO dephasing, LO decoherence thus being the only relevant noise source.

A. Allan variance and phase slips

1. Allan variance

We introduce the (dimensionless) fractional time-averaged frequency offset

$$y_n(T, \mu_n) = \frac{\theta_n(T) - \Theta(\mu_n)}{\omega_0 T}, \tag{16}$$

given by the difference between the accumulated rotation angle $\theta_n(T) = \int_{(n-1)T}^{nT} dt\ \delta\omega_{\rm LO}(t)$ during the nth Ramsey cycle and its estimate value $\Theta(\mu_n)$ [29]. We quantify the stability of the clock by the fluctuations of the average $\frac{1}{n_c}\sum_{n=1}^{n_c} y_n(T,\mu_n)$ in n_c Ramsey cycles. In particular, the two-points variance (commonly indicated as the Allan variance [1–3,30])

$$\sigma_{n_c}^2 = \frac{1}{2n_c(n_c-1)}\sum_{n=1}^{n_c-1}(y_{n+1}-y_n)^2 \tag{17}$$

is generally considered to estimate the stability due to stochastic noise since constant systematic errors cancel in Eq. (17).

In the absence of strong constant biases (such as those induced by phase slips), correlations between consecutive measurements of y_n can be generally neglected: $\sum_{n=1}^{n_c-1} y_{n+1}y_n \ll \sum_{n=1}^{n_c-1} y_n^2 \approx \sum_{n=1}^{n_c-1} y_{n+1}^2$. Indeed, although the frequency noise may be correlated, the phase estimations are uncorrelated, which makes the correlations between y_n and y_{n+1} negligible when compared to their fluctuations. We thus have

$$\sigma_{n_c}^2 = \frac{1}{(n_c-1)n_c}\sum_{n=1}^{n_c-1} y_n^2. \tag{18}$$

For sufficiently large n_c, we write Eq. (18) as a statistical average, that we indicate as $\mathcal{E}_{\mu,\theta}$, over both random frequency fluctuations (or, equivalently, random values of θ) and random measurement results μ:

$$\sigma_{n_c}^2 = \frac{1}{\omega_0^2 T^2 n_c}\mathcal{E}_{\mu,\theta}\{[\theta(T)-\Theta(\mu)]^2\}. \tag{19}$$

Introducing the joint probability distribution $P_T(\mu,\theta)$, which depends, in general, on the Ramsey time T, we can write Eq. (19) as

$$\sigma_{n_c}^2 = \frac{1}{\omega_0^2 T^2 n_c}\int d\theta \sum_{\mu} P_T(\mu,\theta)[\theta-\Theta(\mu)]^2. \tag{20}$$

Finally, using the basic conditional probability relation $P_T(\mu,\theta) = P(\mu|\theta)P_T(\theta)$ and $\sum_\mu P(\mu|\theta)[\theta-\Theta(\mu)]^2 = [\Delta\Theta(\theta)]^2 + [\theta-\bar\Theta(\theta)]^2$, we arrive at the equation

$$\sigma_{n_c}^2 = \frac{c_T^2}{\omega_0^2 T^2 n_c}, \tag{21}$$

where

$$c_T^2 = \int d\theta\, P_T(\theta)\,[[\Delta\Theta(\theta)]^2 + [\theta-\bar\Theta(\theta)]^2] \tag{22}$$

is a weighted average of the mean square error. Equation (21) links $\sigma_{n_c}^2$, the estimator variance $(\Delta\Theta)^2$ and the bias $|\theta-\bar\Theta(\theta)|$. In particular, c_T^2 fulfils the Cramér-Rao bound [31,32]

$$c_T^2 \geqslant \int d\theta\, P_T(\theta)\left[\frac{1}{F(\theta)}\left(\frac{d\bar\Theta}{d\theta}\right)^2 + [\theta-\bar\Theta(\theta)]^2\right], \tag{23}$$

where $F(\theta) = \sum_\mu \frac{1}{P(\mu|\theta)}\left(\frac{P(\mu|\theta)}{d\theta}\right)^2$ is the Fisher information. The bound (23) holds for any estimator $\Theta(\mu)$. For unbiased estimators, namely $\bar\Theta(\theta)=\theta$, the bound (23) equals the weighted average of the inverse Fisher information, $c_T^2 \geqslant \int d\theta\, P_T(\theta)/F(\theta)$. By combining Eqs. (21) and (23) we obtain a lower bound to the Allan variance, although its saturation is not guaranteed, in general. The optimization of $F(\theta)$ over all possible positive operator-valued measure defines the quantum Fisher information, $F(\theta) \leqslant F_Q(\theta)$ [33,34], that depends only on the probe state and interferometer transformation. We thus obtain $c_T^2 \geqslant \int d\theta\, P_T(\theta)/F_Q(\theta)$ for unbiased estimators although the saturation of the bound is not guaranteed since the optimal measure for which the equality $F(\theta) = F_Q(\theta)$ holds depend, in general, on θ [35].

2. Phase slips

Equation (21) gives the Allan variance for a sequence of n_c Ramsey cycles in the absence of phase slips, namely if $|\theta_n| \leqslant \ell$ for $n = 1,\dots,n_c$, where 2ℓ indicates the total width of the inversion region (e.g., $\ell = \pi/2$ for the single Ramsey interferometer, see Sec. II A). If a phase slip occurs at the nth Ramsey cycle, namely $|\theta_n| > \ell$, the estimation method is biased. It is generally unlikely that the frequency can be stabilized around ω_0 if we further interrogate the LO. Instead, additional phase slips may occur, which further increase the estimation bias and make an analytical calculation of the Allan variance cumbersome [36]. In the following, to avoid numerical instabilities, the LO is stopped after the occurrence of a single phase slip. In this case, the number of Ramsey cycles n_c during which no phase slip occurs is thus a stochastic variable. Let us thus indicate as $P_T(n_c)$ the probability that a phase slip occurs at the n_cth Ramsey cycle. This is given by

$$P_T(n_c) = \begin{cases} 1 - 2\int_0^\ell d\theta P_T(\theta) & \text{for} \quad n_c = 1, \\ P_{n_c}(T) \times \prod_{n=1}^{n_c-1}(1-P_n(T)) & \text{for} \quad n_c > 1, \end{cases} \tag{24}$$

where $P_n(T) = 1 - 2\int_{-\ell}^{\ell} d\theta_n P_T(\theta_n)$ is the probability that $|\theta_n(T)| > \ell$.

In the case of a LO with white-noise frequency fluctuations, the values of θ_n are uncorrelated: the probability $P_n(T)$ is thus the same for all Ramsey cycles and it is given by $p(T) = 1 - 2\int_0^l d\theta\ P_T(\theta)$. In this case, Eq. (24) becomes

$$P_T(n_c) = [1-p(T)]^{n_c-1} \times p(T). \tag{25}$$

While the above equations hold for any probability distribution $P_T(\theta)$, a relevant case is the Gaussian

$$P_T(\theta) = \frac{e^{-\frac{\theta^2}{2v_T^2}}}{\sqrt{2\pi\, v_T^2}}, \tag{26}$$

where the variance v_T^2 depends on the interrogation time, as discussed above. In this case we have

$$p(T) = 1 - \mathrm{Erf}\left(\frac{\ell}{\sqrt{2}v_T}\right), \tag{27}$$

where $\mathrm{Erf}(\dots)$ is the error function.

3. General expression for the Allan variance in the presence of phase slips

Let us introduce the total averaging time τ. The quantity $\lfloor \tau/T \rfloor$ indicates the largest integer less than or equal to τ/T and sets the maximum number of Ramsey cycles (neglecting

dead times). Our general expression for the Allan variance is

$$\sigma^2 = Q_T(\lfloor \tau/T \rfloor)\sigma^2_{\lfloor \tau/T \rfloor} + \sum_{n_c=2}^{\lfloor \tau/T \rfloor} P_T(n_c)\sigma^2_{n_c}. \tag{28}$$

The first term corresponds to the case where no phase slip happens in any of the $\lfloor \tau/T \rfloor$ Ramsey cycles: this occurs with probability $Q_T(\lfloor \tau/T \rfloor) = \prod_{n=1}^{\lfloor \tau/T \rfloor}[1 - P_n(T)]$. The second term in Eq. (28) corresponds to a statistical average of $\sigma^2_{n_c}$ with $P_T(n_c)$ being the probability that a phase slip at the n_cth Ramsey cycle, as given in Eq. (27). The sum starts from $n_c = 2$ since at least two Ramsey cycles are required to calculate the Allan variance according to Eq. (17). Finally, using Eq. (21), we find

$$\sigma^2 = \frac{c_T^2}{\omega_0^2 T^2}\left(\frac{Q_T(\lfloor \tau/T \rfloor)}{\lfloor \tau/T \rfloor} + \sum_{n_c=2}^{\lfloor \tau/T \rfloor} \frac{P_T(n_c)}{n_c} \right). \tag{29}$$

This equation is characterized by two limits. If the interrogation time T and the ratio τ/T are sufficiently short such that $P_T(n_c) \approx 0$ for $n_c = 1, \ldots, \lfloor \tau/T \rfloor$ and thus $Q_T(\lfloor \tau/T \rfloor) \approx 1$, then the effect of phase slips is negligible and we obtain

$$\sigma^2 = \frac{c_T^2}{\omega_0^2 T \tau}, \tag{30}$$

where we approximated $T \times \lfloor \tau/T \rfloor \approx \tau$. This equation recovers the characteristic scaling $\sigma^2 \sim 1/(T\tau)$. In the opposite regime, when the term $Q_T(\lfloor \tau/T \rfloor)/(\lfloor \tau/T \rfloor)$ is negligible (e.g., in the limit $\tau/T \to \infty$), we obtain

$$\sigma^2 = \frac{c_T^2}{\omega_0^2 T^2} \sum_{n_c=2}^{\lfloor \tau/T \rfloor} \frac{P_T(n_c)}{n_c}. \tag{31}$$

In this case, phase slips dominate the calculation of the Allan variance and we find that σ^2 does not scale with τ: changing the total averaging time has no effect on the Allan variance since there is a substantial probability that a phase slip occurs for $n_c \leqslant \lfloor \tau/T \rfloor$.

B. Allan variance and phase slips for the single-Ramsey clock protocol

In Fig. 3 we plot the Allan variance for the clock protocol based on a single Ramsey interferometer, as a function of τ/T. Different symbols are results of *ab initio* numerical simulations for different fixed values of Ramsey time T. For values of θ inside the inversion region $[-\ell, \ell]$ ($\ell = \pi/2$ in this case), we have $|\theta - \bar{\Theta}_A| \ll \Delta\Theta_A(\theta) = 1/\sqrt{N_t}$, see Fig. 2(a), and thus $c_T^2 = 1/N_t$. In particular, according to Eq. (30), for sufficiently short values of τ/T, we recover the standard quantum limit (SQL) [5,37,38]

$$\sigma^2 = \frac{1}{\omega_0^2 N_t T \tau}. \tag{32}$$

For large values of τ/T, the Allan variance is characterized by a saturation, as predicted by Eq. (31),

$$\sigma^2 = \frac{1}{\omega_0^2 N_t T^2} \sum_{n_c=2}^{\lfloor \tau/T \rfloor} \frac{P_T(n_c)}{n_c}. \tag{33}$$

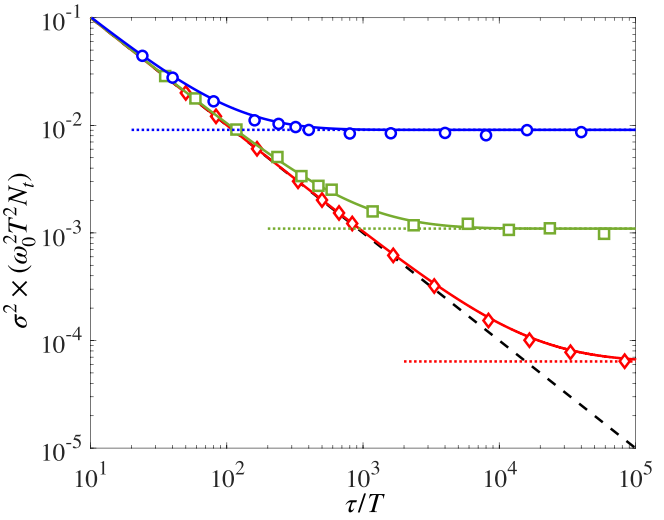

FIG. 3. Allan variance as a function of τ/T for white LO noise and obtained with a clock based on a single Ramsey interferometer. Symbols are results of *ab initio* numerical simulation for different values of the Ramsey time: $\gamma_{\rm LO}T = 0.25$ (blue circles), $\gamma_{\rm LO}T = 0.17$ (green squares), and $\gamma_{\rm LO}T = 0.12$ (red diamonds). Solid lines are Eq. (34), the dashed line is the SQL, Eq. (32), while the dotted lines are the asymptotic $\tau/T \to +\infty$ prediction of Eq. (35). Here $N_t = 1000$

For white noise, Eq. (29) can be calculated using Eq. (25) and $c_T^2 = 1/N_t$. This gives

$$\sigma^2 = \frac{1}{\omega_0^2 T^2 N_t}\left[\frac{p(T)}{1-p(T)} \sum_{n_c=2}^{\lfloor \tau/T \rfloor} \frac{[1-p(T)]^{n_c}}{n_c} + \frac{[1-p(T)]^{\lfloor \tau/T \rfloor}}{\lfloor \tau/T \rfloor} \right], \tag{34}$$

where we used $Q_T(\lfloor \tau/T \rfloor) = [1-p(T)]^{\lfloor \tau/T \rfloor}$ and $p(T)$ is calculated according to Eq. (27). In the limit $\tau/T \to +\infty$, Eq. (34) becomes

$$\sigma^2 = \frac{1}{\omega_0^2 T^2 N_t}\left[\frac{p(T)}{1-p(T)} \log \frac{1}{p(T)} - p(T) \right]. \tag{35}$$

As shown in Fig. 3, the numerical results agree very well with the analytical prediction [solid lines, given by Eq. (34)]. The dotted lines is the asymptotic plateau Eq. (35).

To study the Allan variance as a function of the Ramsey time T, we fix the total averaging time τ. In this case, by increasing T, we find a transition between Eqs. (32) and (33): while Eq. (32) predicts that the Allan variance decreases as $\sigma^2 \sim 1/T$, Eq. (33) increases as a function of T. The bending knee of the Allan variance (that identifies the absolute stability of the clock) is clearly shown in Figs. 4(a) and 4(b), obtained for white and flicker LO noise, respectively. The green diamonds are results of *ab initio* numerical simulations. The solid line in Fig. 4(a) is the analytical prediction Eq. (34) for white noise, while for flicker noise [Fig. 4(b)] the solid green line is obtained by calculating $P_T(n_c)$ and $Q_T(\lfloor \tau/T \rfloor)$ numerically (and independently from the numerical simulations of σ^2).

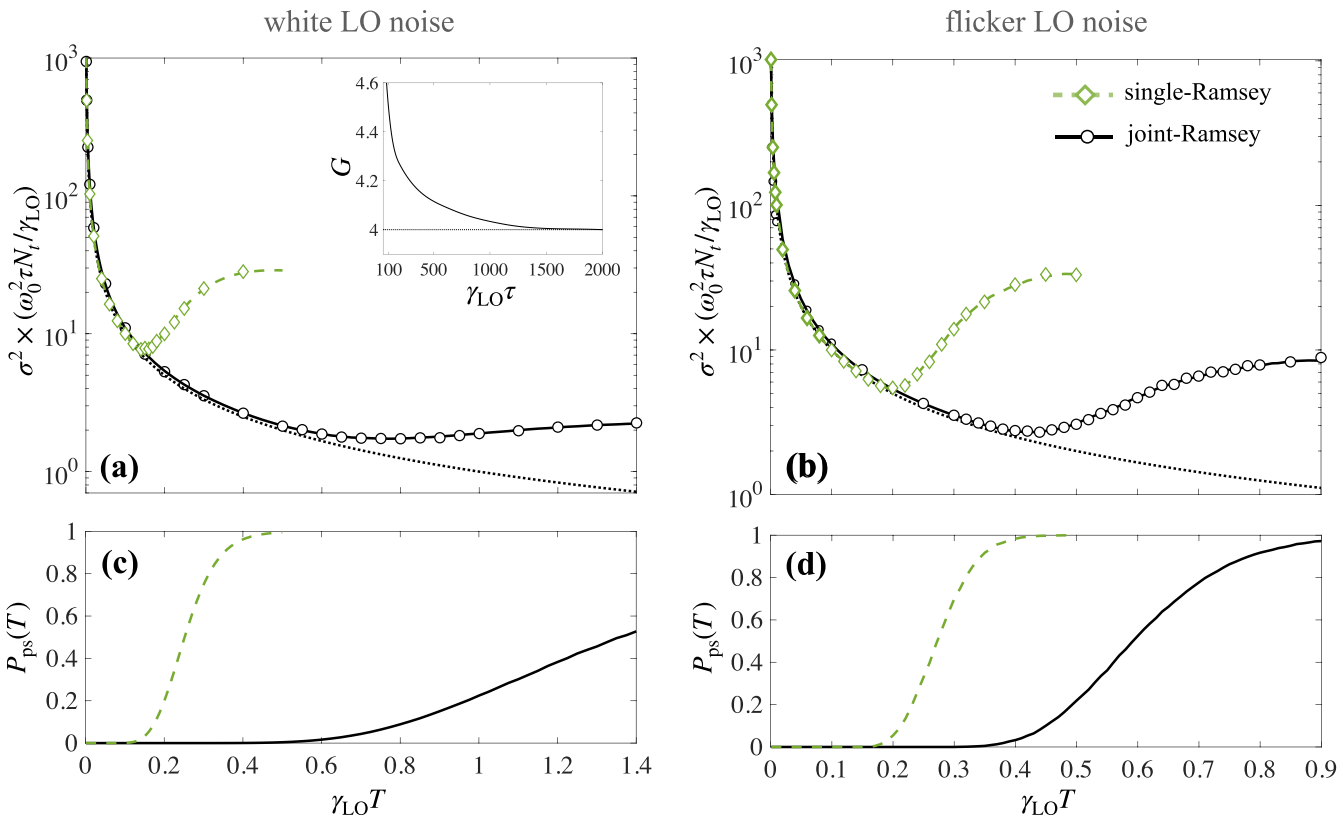

FIG. 4. Allan variance (multiplied by $\omega_0^2\tau N_t/\gamma_{LO}$) as a function of the Ramsey time $\gamma_{LO}T$ for (a) white and (b) flicker LO noise, respectively. Symbols are results of *ab initio* numerical simulations: green diamonds are obtained for a single-Ramsey clock with $N_t = 2000$ particles, while black circles are obtained for a joint-Ramsey clock with 1000 particles in each interferometer ($N_t = 2000$ is the total number of particles used in both clocks). The dotted line in both panels is the SQL, $\sigma^2 = 1/(\omega_0^2 T\tau N_t)$. The solid and dashed lines in both panels are expected results. For the white-noise case, the dashed green line is Eq. (34), while the solid black line is Eq. (38). For the flicker noise, the lines are semi-analytical predictions given by Eq. (29) where the quantities $Q_T(\lfloor\tau/T\rfloor)$, $P_T(n_c)$ and c_T^2 are obtained numerically and independently from the calculation of the Allan variance. The inset of panel (a) shows the gain G defined in Eq. (39) for the white-noise LO case, as a function of the total averaging time $\gamma_{LO}\tau$. The solid line is obtained analytically and shows that the gain in the noiseless case converges to $G = 4$ (dashed line) for large τ. Panels (c) and (d) show the probability of phase slip, Eq. (36), as a function of $\gamma_{LO}T$, for white and flicker noise, respectively. The solid lines in panel (c) is Eq. (37). In all panels, $\gamma_{LO}\tau = 100$.

In Figs. 4(c) and 4(d) we show the overall probability that a phase slip occurs in one of the $\lfloor\tau/T\rfloor$ Ramsey cycles, namely,

$$P_{ps}\big(T, \lfloor\tau/T\rfloor\big) = \sum_{n_c=1}^{\lfloor\tau/T\rfloor} P_T(n_c) = 1 - Q_T(\lfloor\tau/T\rfloor), \qquad (36)$$

as a function of the Ramsey time. Figure 4(c) is obtained for white noise, while in Fig. 4(d) for flicker noise. In the case of white noise, Eq. (36) can be evaluated analytically as

$$P_{ps}(T, \lfloor\tau/T\rfloor) = 1 - [1 - p(T)]^{\lfloor\tau/T\rfloor}, \qquad (37)$$

given by the solid line in Fig. 4(c). We observe that the bending of the Allan variance is obtained when $P_{ps}(T, \lfloor\tau/T\rfloor) \approx 0.05$ (and similarly for flicker noise). It should be noticed that the optimal Ramsey time corresponding to the minimum of the Allan variance has a slight dependence on the total interrogation time τ (in particular, it decreases with τ). This is due to the fact that increasing τ, for a fixed Ramsey time T, the number of cycles increases and thus the probability to have a phase slip increases as well, as shown in Eq. (37). In particular, in the limit $\tau/T \to \infty$, we have $P_{ps}(T, \lfloor\tau/T\rfloor) \to 1$ whenever $p(T) > 0$.

C. Allan variance and phase slips for the joint-Ramsey clock protocol

The Allan variance for the joint-Ramsey clock can be obtained following the discussion of Sec. III A. To be explicit, our semi-analytical prediction is given by Eq. (29) with $c_T^2 = \int d\theta\, P_T(\theta)\,[[\Delta\Theta(\theta)]_{AB}^2 + (\theta - \bar{\Theta}_{AB}(\theta))^2]$. In particular, we consider here the case $N_A = N_B = N$. The major difference with respect to the single-Ramsey clock is the size of the inversion region $[-\ell, \ell]$ that is identified here with $\ell = \pi - 4/\sqrt{N}$ (rather than $\ell = \pi/2$ as in the case of a single Ramsey interferometer). The factor of $4/\sqrt{N}$ guarantees a small probability of biased estimation close to the $\theta = \pm\pi$, see Fig. 2(b). In particular, for the white-noise case,

we have

$$\sigma^2 = \frac{c_T^2}{\omega_0^2 T^2}\left[\frac{p(T)}{1-p(T)}\sum_{n_c=2}^{\lfloor \tau/T \rfloor}\frac{[1-p(T)]^{n_c}}{n_c} + \frac{[1-p(T)]^{\lfloor \tau/T \rfloor}}{\lfloor \tau/T \rfloor}\right], \tag{38}$$

with $p(T)$ given in Eq. (27) with $\ell = \pi - 4/\sqrt{N}$.

In Figs. 4(a) and 4(b) we show the results of numerical calculations of the Allan variance for the joint-Ramsey clock, in the case of white and flicker LO noise, respectively. In the figure, the single-Ramsey clock (green diamonds) and the joint-Ramsey scheme (black circles) are compared for the same total number of particles N_t (in the joint scheme the total number of particles is $N_t = 2N$). Notice that the black circles stay slightly above the dashed line, giving the SQL $\sigma^2_{\rm SQL} = 1/(\omega_0^2 T \tau N_t)$. This effect is due to the mean square error $(\Delta\Theta_{AB})^2 + (\theta - \bar{\Theta}_{AB}(\theta))^2$, which is relevant to calculate the quantity c_T^2 in Eq. (29), being slightly above $1/N_t$ for θ close to 0 and $\pm\pi/2$, see Fig. 2(b). This is a minor effect that can nevertheless be seen in the numerical simulations. For both white and flicker noise, the numerical results are well reproduced by semi-analytical findings (solid lines) obtained using Eq. (29).

As shown in Figs. 4(a) and 4(b), using the joint-Ramsey interrogation, the minimum of the Allan variance is reached for longer interrogation times, with respect to the single-Ramsey clock. This corresponds to an increase of the absolute stability that can be quantified by the gain factor

$$G = \frac{(\min_T \sigma^2)_{\rm single}}{(\min_T \sigma^2)_{\rm joint}}, \tag{39}$$

given by the ratio between the Allan variance for the single-Ramsey clock (with N_t particles) and that of the joint protocol (with N particles in each ensemble, $N_t = 2N$ in total), each optimized with respect to the Ramsey time. For while LO noise we obtain that $G \approx 4$. In particular, the inset of Fig. 4(a) shows G as a function of $\gamma_{\rm LO}\tau$. For $\gamma_{\rm LO}\tau = 100$ corresponding to the results shown in the main panel of Fig. 4(a), we obtain $G \approx 4.5$. For large values of τ we obtain that G converges to the value 4. For flicker noise, we obtain $G \approx 2$ with a weak dependence on τ (not shown). The increase of stability obtained with the joint clock is directly related to the smaller probability of phase slips, as shown in Figs. 4(c) and 4(d).

IV. IMPACT OF POSSIBLE IMPERFECTIONS

In this section we consider the impact of possible experimental imperfections in the implementation of the joint-Ramsey scheme. Specifically, we release the assumption of the perfect $\pi/2$ shift between the coherent spin states in the two interferometers and also consider the impact of the number of particles' fluctuations and dead time.

A. Imperfect alignment of the probe states

We study here the joint Ramsey scheme of Fig. 1(a) where the probe state of the Ramsey B interferometer is given by the statistical mixture

$$\hat{\rho}_B = \int d\epsilon\, P(\epsilon)\, |\psi_B\rangle_\epsilon \langle\psi_B|, \tag{40}$$

where $|\psi_B\rangle_\epsilon = (e^{-i(\pi/2-\epsilon)/2}|\uparrow\rangle + e^{i(\pi/2-\epsilon)/2}|\downarrow\rangle)^{\otimes N_B}/2^{N_B/2}$, and $P(\epsilon) = e^{-\epsilon^2/(2s_\epsilon^2)}/\sqrt{2\pi s_\epsilon^2}$. Here, ϵ is a stochastic value that accounts for a misalignment of the probe state along the y axis in the Bloch sphere. Equation (40) reduces to Eq. (7) for $s_\epsilon = 0$. The effect of an imperfect (stochastic) alignment is equivalent to that of a stochastic relative phase shift between the two interferometers due, for instance, to fluctuations of the clocks' atomic frequencies.

Figures 5(a) and 5(b) show the gain Eq. (39) as a function of s_ϵ for white and flicker LO noise, respectively. As shown in the inset of Fig. 5(b), the main effect of the imperfection in the state preparation is to increase the Allan variance, while the optimal Ramsey time remains approximately constant. The gain factor G decreases while increasing s_ϵ. The

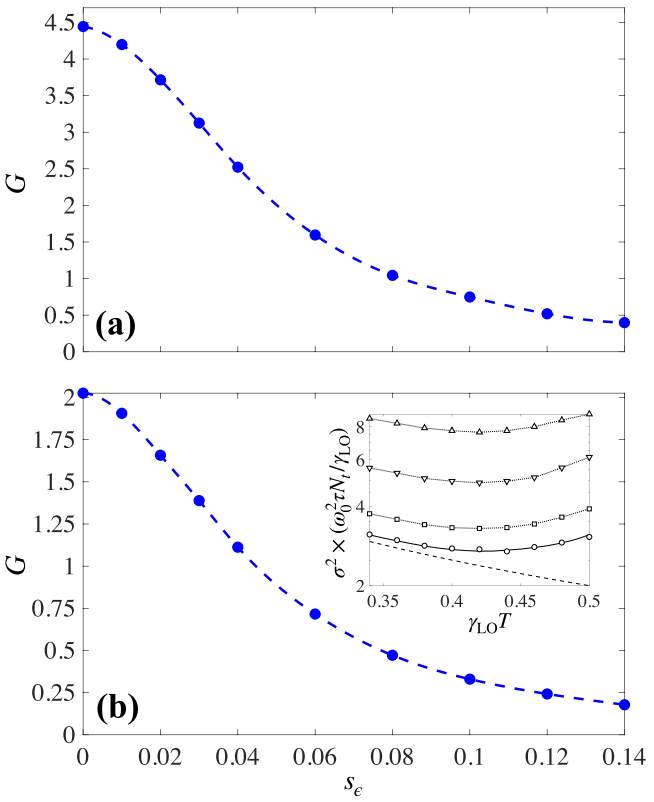

FIG. 5. Absolute stability gain G, Eq. (39), as a function of the parameter s_ϵ quantifying the imperfect alignment of the two probe states of the joint-Ramsey clock. Panel (a) is obtained for white LO noise, while panel (b) for flicker noise. In each panel, blue dots are results of numerical simulations, the dashed line is a guide to the eye. The inset of panel (b) shows the Allan variance as a function of the Ramsey time $\gamma_{\rm LO}T$. Different symbols are obtained for different values of ϵ: $s_\epsilon = 0$ (circles), $s_\epsilon = 0.02$ (squares), $s_\epsilon = 0.04$ (downward-pointing triangle), and $s_\epsilon = 0.06$ (upward-pointing triangle). The solid line is Eq. (29), the dotted lines are a guide to the eye, and the dashed line is the SQL. In all panels $\gamma_{\rm LO}\tau = 100$ and the total number of particles is $N_t = 2000$.

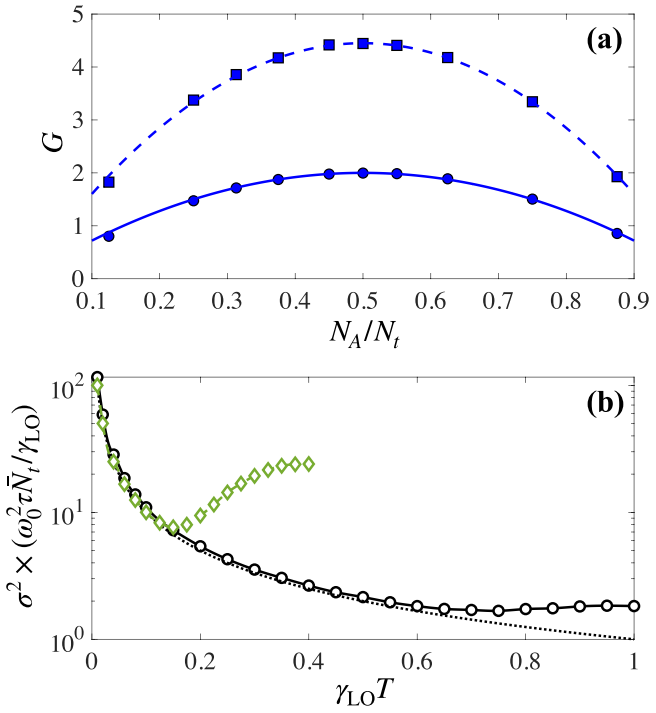

FIG. 6. (a) Stability gain G, Eq. (39), as a function of N_A/N_t. Symbols are results of numerical simulations: squares (dots) are obtained for white (flicker) LO noise. The lines are Eq. (41). Here $N_t = 2000$. (b) Allan variance as a function of the Ramsey time in the presence of the number of particles fluctuations. Symbols are results of numerical simulations. Diamonds are obtained for a single Ramsey clock with $\bar{N} = 2000$ and $\Delta N = \sqrt{\bar{N}}$. Circles corresponds to a the joint clock scheme with $\bar{N}_A = \bar{N}_B = 1000$ and $\Delta N_{A,B} = \sqrt{\bar{N}_{A,B}}$. The dotted line is the SQL, $\sigma^2 = 1/(\omega_0^2 T \tau \bar{N}_t)$ with $\bar{N}_t = 2000$. Here $\gamma_{LO}\tau = 100$.

condition to have values $G > 1$ is more stringent in the case of flicker LO noise.

B. Number of particles fluctuations

When the number of particles in the two interferometers is different, Eq. (13) predicts

$$G \propto \frac{N_A}{N_t}\left(1 - \frac{N_A}{N_t}\right), \tag{41}$$

which has the optimal working point when $N_A = N_B$. Figure 6(a) reports the results of numerical simulations showing the gain factor G as a function of N_A/N_t. The different symbols refer to white (squares) and flicker (dots) noise. They agree well with the corresponding line given by Eq. (41).

We further investigate the situation where the number of particles in each interferometer fluctuates from shot to shot. In this case, we replace the coherent spin states (2) and (7) by a Gaussian statistical distribution of coherent spin states of $N_{A,B}$ particles, with mean $\bar{N}$ and fluctuations ΔN (assumed to be the same for the two interferometers). The number of particles' fluctuations have two main effects. First, they increase the rate of estimation biases close to $\pm\pi$. We take into account this effect by identifying the half-size of the inversion region as $\ell = |\pi - 4/\sqrt{\bar{N} + 4\Delta N}|$, where the factor of 4 is used to avoid biases around $\theta \approx \pm\pi$ (see discussion above). Second, the number of particles in each interferometer fluctuates from shot to shot, which decreases the sensitivity according to Eqs. (13) and (41). Both effects are negligible for $\Delta N \ll \bar{N}$. This is confirmed in Fig. 6(b), where we show the Allan variance as a function of $\gamma_{LO}T$, by taking $\Delta N = \sqrt{\bar{N}}$. We compare the single clock with $\bar{N} = \bar{N}_t = 2000$ (green diamonds) with the joint clock scheme with $\bar{N}_A = \bar{N}_B = \bar{N}_t/2$. As we see, the Allan variance follows the behavior of Fig. 4(a): still we obtain a gain factor $G \sim 4$.

C. Dead times

In common experimental realizations of atomic clocks, the interrogation of the atoms during a Ramsey time T is followed by a dead time T_D required for experimental operations such as detection, loading, laser cooling, and state preparation. During the dead time the LO is not interrogated by the atoms. Nevertheless, the dead time can be completely eliminated by antisynchronous interrogation of two atomic ensembles [39–43], where the two ensembles essentially form one clock with no dead time.

There are two main consequences associated to the dead time. (i) The number of Ramsey cycles, for given Ramsey time T and given total interrogation time τ, is now given by τ/T_C and decreases as T_D increases, where $T_C = T + T_D$ is the total cycle time. The main effect associated to the decrease of the number of Ramsey cycles is to replace $\lfloor \tau/T \rfloor$ in Eq. (28) by $\lfloor \tau/T_C \rfloor$. For instance, the SQL, Eq. (32), is now replaced by [5,37]

$$\sigma^2_{SQL} = \frac{1}{\omega_0^2 T^2 N}\frac{T_C}{\tau}. \tag{42}$$

The smaller number of cycles is also associated to a slight decrease of probability of phase slips, as discussed above. This is however a minor effect. (ii) The other, more subtle, phenomenon is the so-called Dick effect [44]. In the presence of a dead time, Eq. (16) is replaced by

$$y_n(T, \mu_n) = \frac{\theta_n(T) + \tilde{\theta}_n(T_D) - \Theta(\mu_n)}{\omega_0 T}, \tag{43}$$

where $\theta_n(T) = \int_{(n-1)T_C}^{(n-1)T_C+T} dt\ \delta\omega_{LO}(t)$, is the phase accumulated during the interrogation time T at the nth Ramsey cycle and $\tilde{\theta}_n(T_D) = \int_{(n-1)T_C+T}^{nT_C} dt\ \delta\omega_{LO}(t)$ is the phase that accumulates during the dead time. The quantity $\Theta(\mu_n)$ is an estimate of $\theta_n(T)$ only. In other words, the average phase $\theta_n(T_D)$ that accumulates during the dead time T_C is not estimated by the inteferometer. Effectively, the dead time results in the lack of information about the frequency spectrum of the LO due to the sampling process [44–48]. According to the authors of Refs. [44,45], the Dick effect alone is associated to an Allan variance

$$\sigma_D^2 = \frac{1}{\tau}\sum_{k=1}^{+\infty} S(k/T_C)\left(\frac{\sin(k\pi d)}{k\pi d}\right)^2, \tag{44}$$

depending on the power spectral density of the free-running LO taken at Fourier frequencies k/T_C, where $d = T/T_C$. More

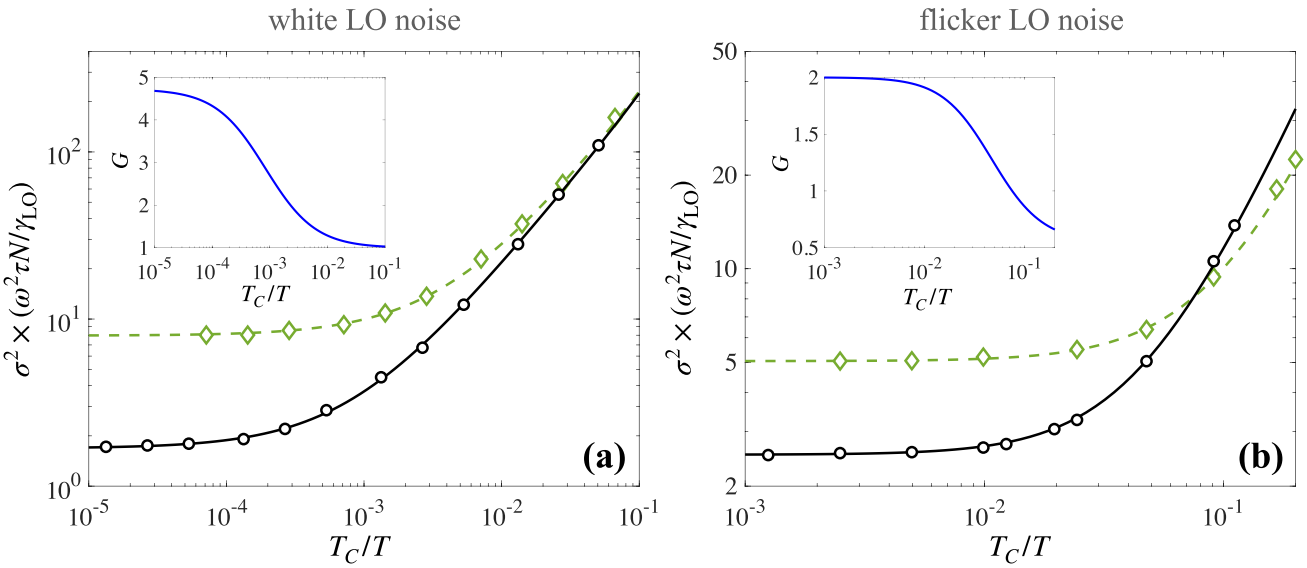

FIG. 7. Allan variance as a function of the total cycle time time $T_C = T + T_D$ for (a) white and (b) flicker noise, respectively. Here the Ramsey time T is set to that minimizing the Allan variance for $T_D = 0$, see Fig. 4. In each panel, diamonds (circles) refer to results of numerical simulations for the single (joint) Ramsey clock scheme. Lines are the corresponding analytical behavior (see text). The inset shows the stability gain factor Eq. (39), calculated from the analytical functions. Here the total number of particles is $N_t = 2000$, the averaging time is $\tau/T_C = 100$.

explicitly, for white LO noise, Eq. (44) becomes

$$\sigma_D^2 = \frac{\gamma_{LO}}{\omega_0^2 \tau} \frac{2}{d^2} \sum_{k=1}^{+\infty} \frac{\sin^2(k\pi d)}{\pi^2 k^2}, \tag{45}$$

while for flicker noise, we have

$$\sigma_D^2 = \frac{\gamma_{LO}}{\omega_0^2 \tau} \frac{\gamma_{LO}}{2\chi \log 2} \frac{T}{d^2} \sum_{k=1}^{+\infty} \frac{\sin^2(k\pi d)}{\pi^2 k^3}. \tag{46}$$

Following Ref. [49], we assume that the Allan variance associated to the Dick effect adds to the Allan variance due to the atomic interrogation. More explicitly, Eq. (29), is now replaced by the sum of the two contributions:

$$\sigma^2 = \frac{c_T^2}{\omega_0^2 T^2} \left(\frac{Q_T(\lfloor \tau/T_C \rfloor)}{\lfloor \tau/T_C \rfloor} + \sum_{n_c=2}^{\lfloor \tau/T_C \rfloor} \frac{P_T(n_c)}{n_c} \right) + \sigma_D^2, \tag{47}$$

which, as discussed above, can be adapted for the single- or the joint-Ramsey interrogation.

In Fig. 7 we show the results of numerical simulations of the different clock protocols in the presence of a dead time T_D. The main panels show the Allan variance of the joint-Ramsey clock as a function of T_C/T. Here T is the optimal Ramsey time minimizing the Allan variance in the case $T_D = 0$, as shown in Fig. 4. The symbols are results of numerical simulations, the lines are analytical predictions, e.g., Eqs. (47) and (44) for the joint protocol. The insets show the gain factor Eq. (39) as calculated from the analytical behavior. The Allan variance rapidly increases with T_D. As a direct consequence, the gain factor decreases to values $G < 1$ for $T_D/T \sim 10^{-2}$ for white LO noise [Fig. 4(a)] and $T_D/T \sim 5 \times 10^{-2}$ for flicker noise [Fig. 4(b)].

V. JOINT-RAMSEY INTERROGATION COMBINED WITH SPIN SQUEEZING

In the following, we combine the joint interrogation method discussed above with the approach proposed in Ref. [26] (see also Ref. [50]). The overall clock scheme is shown in Fig. 8. It consists of three Ramsey interferometers operating in parallel with the LO now interrogating three atomic ensembles. We assume that the three ensembles have the same number of particles N: this is relevant for atomic clocks where, to increase the stability, one wants to use atomic ensembles that have maximum possible number of atoms, eventually limited by spatial constraints or the onset of decoherence affects associated to the large density. The input of Ramsey A is given by Eq. (2), the input of Ramsey B is given by Eq. (7), while the input of Ramsey C is

$$|\psi_C\rangle = \mathcal{N} \sum_{\mu=-N/2}^{N/2} e^{-\mu^2/(s^2 N)} |\mu\rangle_y, \tag{48}$$

where $|\mu\rangle_y$ are the eigenstates of $\hat{J}_y$ with eigenvalues $\mu = -N/2, -N/2+1, \ldots, N/2$, $\mathcal{N}$ provides the normalization and the parameter s sets the variance $(\Delta \hat{J}_y)^2 = s^2 N/4$. For $s < 1$ the Eq. (48) is spin squeezed [27,51–55], with metrological squeezing coefficient $\xi^2 = N(\Delta \hat{J}_y)^2/\langle \hat{J}_x \rangle \approx s^2 e^{1/(s^2 N)} < 1$ [26,50].

In the scheme of Fig. 8, the accumulated phase rotation angle θ is the same for all probe states. The joint interrogation of the first two ensembles (using the method discussed in Sec. III C) provides a first estimate, $\Theta_{AB}(\mu_A, \mu_B)$, of the true value $\theta \in [-\pi, \pi]$, depending on the measurement results μ_A and μ_B, see Eqs. (10) and (11). The phase feedback consists of a rotation of the spin-squeezed state around the y axis by an angle $\Theta_{AB}(\mu_A, \mu_B)$. Overall, the spin-squeezed state (48)

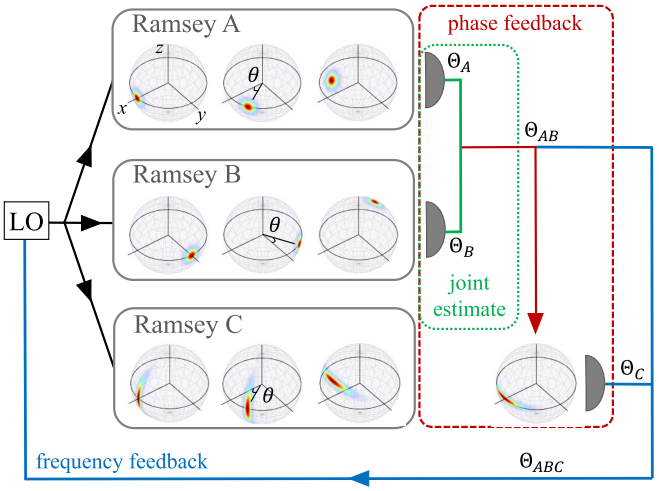

FIG. 8. Clock scheme combining joint-Ramsey interrogation and spin squeezing. It consists of three Ramsey interferometers. The first two interferometers (Ramsey A and Ramsey B) use the coherent spin states (2) and (7), respectively. The two estimates Θ_A and Θ_B are combined according to the discussion in Sec. III C (green dotted square and lines). The joint estimate Θ_{AB}, Eq. (10) is used, via a phase feedback (red dashed square and lines), to bring the spin-squeezed state toward its optimal working point, on the equator of the Bloch sphere. The sum of Θ_{AB} and Θ_C giving Θ_{ABC}, Eq. (51), is used to steer the LO frequency via a frequency feedback (blue line).

is rotated by an angle $\theta_C(\mu_A, \mu_B) = \theta - \Theta_{AB}(\mu_A, \mu_B)$ around the y axis, before the final readout. The feedback rotation aligns the spin-squeezed state along the equator of the generalized Bloch sphere, see Fig. 8, where the state is maximally sensitive [26,56–58]. The Ramsey signal for the third clock is

$$\langle \hat{J}_z(\theta_C)\rangle_{\rm out} = \langle \hat{J}_x\rangle_{\rm in} \sin\theta_C. \tag{49}$$

A measurement of the relative number of particles in the third clock (with result μ_C) leads to the estimate

$$\Theta_C(\mu_C) = \arcsin\frac{\mu_C}{\langle \hat{J}_x\rangle_{\rm in}} \tag{50}$$

of θ_C. This value is added to $\Theta_{AB}(\mu_A, \mu_B)$ giving the estimate

$$\Theta_{ABC}(\boldsymbol{\mu}) = \Theta_{AB}(\mu_A, \mu_B) + \Theta_C(\mu_C) \tag{51}$$

of θ, where $\boldsymbol{\mu} \equiv \{\mu_A, \mu_B, \mu_C\}$.

In Fig. 9(a) we plot the bias, $|\theta - \bar{\Theta}_{ABC}(\theta)|$ as a function of θ, where $\bar{\Theta}_{ABC}(\theta) = \mathcal{E}_{\boldsymbol{\mu}|\theta}\{\Theta_{ABC}(\boldsymbol{\mu}\}$, $\mathcal{E}_{\boldsymbol{\mu}|\theta}\{\ldots\} = \sum_{\boldsymbol{\mu}} \Theta_{ABC}(\boldsymbol{\mu})P(\boldsymbol{\mu}|\theta)\ldots$ indicates the statistical averaging, and $P(\boldsymbol{\mu}|\theta) = P(\mu_A|\theta)P(\mu_B|\theta)P[\mu_C|\theta - \Theta_{AB}(\mu_A, \mu_B)]$. In Fig. 9(b) we plot the mean squared error $\mathcal{E}_{\boldsymbol{\mu}|\theta}\{[\Theta_{ABC}(\boldsymbol{\mu}) - \theta]^2\}$, of Θ_{ABC}. Taking into account Eq. (51), we obtain

$$\mathcal{E}_{\boldsymbol{\mu}|\theta}\{[\Theta_{ABC}(\boldsymbol{\mu}) - \theta]^2\} = \sum_{\mu_A,\mu_B} P(\mu_A|\theta)P(\mu_B|\theta) \times \mathcal{E}_{\mu_C|\theta}\{[\Theta_C(\mu_C) - \theta_C(\mu_A, \mu_B)]^2\}. \tag{52}$$

The rotation angle θ_C is a stochastic variable, depending on the measurement results μ_A and μ_B. We can thus introduce

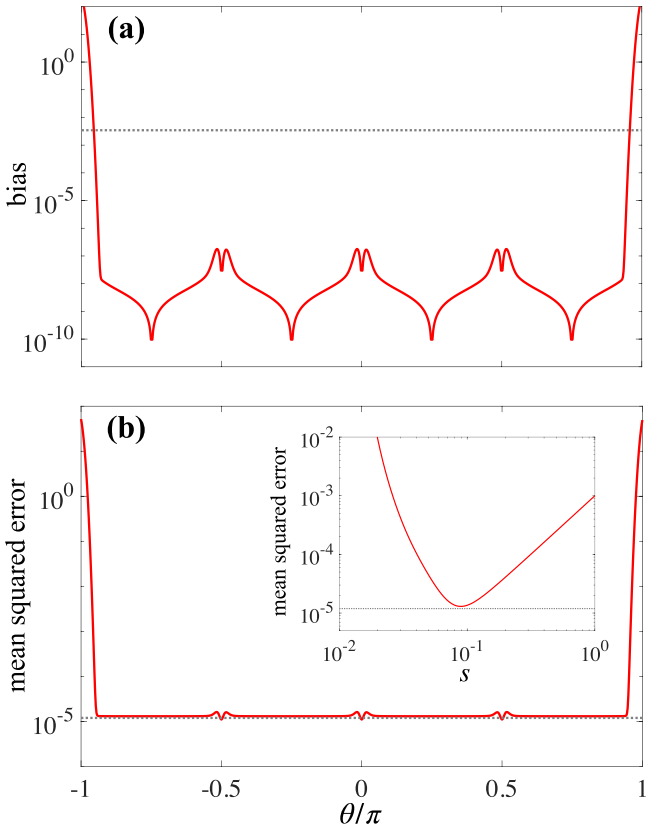

FIG. 9. (a) Bias $|\theta - \bar{\Theta}_{ABC}(\theta)|$ and (b) mean squared error as a function of θ (solid red lines). Results are obtained for the squeezing parameter $s^2_{\rm opt} = 1/(2N^2)^{1/3}$ and $N = 1000$. The inset shows Eq. (56) as a function of the squeezing parameter. In panel (b) and in the inset, the dotted line is Eq. (58). In panel (a), the dotted line is the square root of Eq. (58).

the distribution $P(\theta_C|\theta) = \sum_{\mu_A,\mu_B} P(\mu_A|\theta)P[\mu_B|\theta)\delta(\theta_C - \theta_C(\mu_A, \mu_B)]$, where δ is the Dirac delta function, and write

$$\mathcal{E}_{\boldsymbol{\mu}|\theta}\{[\Theta_{ABC}(\boldsymbol{\mu}) - \theta]^2\} = \int d\theta_C P(\theta_C|\theta)\mathcal{E}_{\mu_C|\theta_C}\{[\Theta_C(\mu_C) - \theta_C]^2\}, \tag{53}$$

The mean squared error of Θ_{ABC} is thus given by a weighted average of the mean squared error of Θ_C. Equation (53) can be decreased thanks to the spin squeezing of $|\psi_C\rangle$, provided that $P(\theta_C|\theta)$ is sufficiently narrow. To quantify this effect we first write $\mathcal{E}_{\mu_C|\theta_C}[[\Theta_C(\mu_C) - \theta_C]^2] = (\Delta\Theta_C)^2 + (\theta_C - \bar{\Theta}_C(\theta_C))^2$, where $\bar{\Theta}_C(\theta_C)$ and $(\Delta\Theta_C)^2$ are, respectively, the statistical mean value and variance of the estimator Θ_C. We then calculate the estimator variance $(\Delta\Theta_C)^2$ via error propagation, obtaining

$$(\Delta\Theta_C)^2 \approx \frac{(\Delta\hat{J}_z(\theta_C))^2_{\rm out}}{(d\langle \hat{J}_z(\theta_C)\rangle_{\rm out})/d\theta_C)^2} = \frac{(\Delta\hat{J}_y)^2_{\rm in}}{\langle \hat{J}_x\rangle^2_{\rm in}} + \frac{(\Delta\hat{J}_x)^2_{\rm in}}{\langle \hat{J}_x\rangle^2_{\rm in}}\tan^2\theta_C. \tag{54}$$

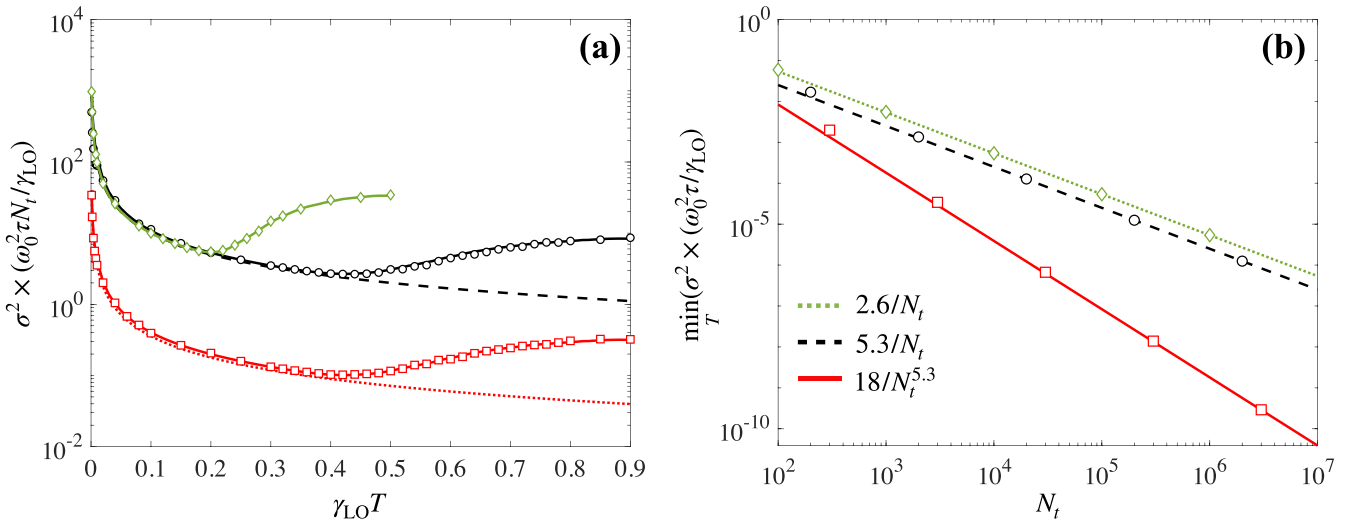

FIG. 10. Panel (a) shows the Allan variance for (i) a single Ramsey clock using a coherent state and $N_t = 3000$ atoms (green diamonds); (ii) a joint Ramsey clocks using two coherent spin states with $N_t/2 = 1500$ atoms each (black circles); (iii) a hybrid clock using two coherent spin states and one optimized spin-squeezed state, each with $N_t/3 = 1000$ atoms each (red squares). Symbols are results of *ab initio* numerical simulations, while the solid lines are semi-analytical predictions (see text). The dashed line is $\sigma^2_{\rm SQL} = 1/(\omega_0^2 T \tau N_t)$. The dotted line is Eq. (59). (b) Scaling of the Allan variance (minimized over the Ramsey time) as a function of N_t for the different clock protocols (i) the single-Ramsey (green diamonds); (ii) the joint-Ramsey (black circles); (iii) the hybrid-Ramsey (red squares). Lines are fits: the dashed and dotted lines are $\sigma^2 = O(1/N_t)$, while the solid line is $\sigma^2 = O(1/N_t^{5/3})$. The numerical results in both panels are obtained for flicker LO noise and $\gamma_{LO}\tau = 100$.

Neglecting the bias, namely taking $|\theta_C - \bar{\Theta}_C(\theta_C)| \ll \Delta\Theta_C$, which is verified numerically, see Fig. 9(a), we obtain

$$\mathcal{E}_{\boldsymbol{\mu}|\theta}\{[\Theta_{ABC}(\boldsymbol{\mu}) - \theta]^2\} = \frac{(\Delta\hat{J}_y)^2_{\rm in}}{\langle \hat{J}_x\rangle^2_{\rm in}} + \frac{(\Delta\hat{J}_x)^2_{\rm in}}{\langle \hat{J}_x\rangle^2_{\rm in}} \int d\theta_C\, P(\theta_C|\theta)\, \theta_C^2, \tag{55}$$

where we used $\tan^2\theta_C \approx \theta_C^2$. Finally, $P(\theta_C|\theta)$ can be taken as a Gaussian distribution with width given by the mean squared error of Θ_{AB}, Eq. (12). As discussed above, Eq. (12) is essentially constant and given by $1/(2N)$ with a slight dependence on θ around 0, $\pm\pi/2$, as shown by the black line in Fig. 2(b). Replacing $P(\theta_C|\theta) = \sqrt{\frac{N}{\pi}} e^{-N\theta_C^2}$ into Eq. (55), we thus obtain

$$\mathcal{E}_{\boldsymbol{\mu}|\theta}\{[\Theta_{ABC}(\boldsymbol{\mu}) - \theta]^2\} = \frac{(\Delta\hat{J}_y)^2_{\rm in}}{\langle \hat{J}_x\rangle^2_{\rm in}} + \frac{(\Delta\hat{J}_x)^2_{\rm in}}{\langle \hat{J}_x\rangle^2_{\rm in}} \frac{1}{2N}. \tag{56}$$

Notice that the average spin moments and variances of the Eq. (48) be calculated analytically for $N \gg 1$ and $s^2 N \gtrsim 1$ [26]: $\langle \hat{J}_x\rangle_{\rm in} = (N/2)e^{-1/(2s^2N)}$, $(\Delta\hat{J}_x)^2_{\rm in} = (N^2/8)(1 - e^{-1/(s^2N)})^2$. These analytical expressions can be replaced into Eq. (56), giving

$$\mathcal{E}_{\boldsymbol{\mu}|\theta}\{[\Theta_{ABC}(\boldsymbol{\mu}) - \theta]^2\} = \frac{4s^2 + (1 - e^{-1/(s^2N)})^2}{4Ne^{-1/(2s^2N)}}. \tag{57}$$

A minimization as a function of the squeezing parameter s gives

$$\min_s \mathcal{E}_{\boldsymbol{\mu}|\theta}\{[\Theta_{ABC}(\boldsymbol{\mu}) - \theta]^2\} \approx \frac{3}{2^{4/3}} \frac{1}{N^{5/3}}, \tag{58}$$

for the optimal value $s^2_{\rm opt} = 1/(2N^2)^{1/3}$, where the last equality holds under the condition $s^2 N \gg 1$ and is obtained by keeping the leading orders in the Taylor expansion of e^{-s^2N}.

A plot of Eq. (56) as a function of the squeezing parameter is shown in the inset of Fig. 9(b). The existence of an optimal squeezing parameter is a direct consequence of the bending of the squeezed state in the Bloch sphere. The bending, quantified by $(\Delta\hat{J}_x)^2_{\rm in}$, increases the output relative number of particles fluctuations for relatively large θ_C, when compared to the single coherent spin-state case [which has $(\Delta\hat{J}_x)^2 = 0$]. This increase of measurement uncertainty corresponds to an increase of phase uncertainty $\Delta\Theta_C$, according to Eq. (54). The squeezed state bends more and more in the Bloch sphere as s decreases. The dashed line in both the main panel and in the inset of Fig. 9(b) is Eq. (58): the agreement with the numerical calculation of the mean square error is excellent apart from the expected wiggles around $\theta = 0$ and $\pm\pi/2$, and the increase close to $\pm\pi$ due to the strong bias of Θ_{ABC} (which, in turn, is due to the bias of Θ_{AB}, as discussed in Sec. II).

Figure 10(a) shows the Allan variance as a function of the interrogation time for three strategies: (i) a single-Ramsey clock in a coherent spin state of $N = 3000$ atoms (green diamonds); (ii) the joint-Ramsey clock strategy using two coherent spin states of $N = 1500$ atoms each (black circles); and (iii) the approach combining joint-Ramsey interrogation and spin squeezing (red squares), using three ensembles of $N = 1000$ atoms each, maximized over s. The symbols are results of *ab initio* numerical simulation of the Ramsey scheme (without using any of the theoretical assumptions considered above). The solid lines are the semi-analytical prediction of Eq. (29). In particular, The dotted red line is the analytical prediction

$$\sigma^2 = \left(\frac{9}{2}\right)^{4/3} \frac{1}{\omega_0^2 T \tau N_t^{5/3}}, \tag{59}$$

that is obtained by neglecting phase slip effects, where $N_t = 3N$. In Fig. 9(d) we show the scaling of the optimal Allan

variance (minimized over Ramsey time T) as a function of the number of particles. The solid line is the numerical fit that confirms the predicted $\sigma^2 = O(1/N_t^{5/3})$ behavior. Furthermore, following Ref. [26], it is possible to extend the scheme of Fig. 8 to a cascade of k squeezed states with decreasing optimal squeezing parameter s and reach a scaling of absolute clock stability $\sigma^2 = O(N_t^{-2+1/3^k})$. The optimization of the number of particles in each ensemble [50] leads to analogous scaling but with improved prefactors.

VI. CONCLUSION

In this paper, we have proposed a joint-Ramsey interrogation method where two coherent spin states initially point along the x and y axes of the generalized Bloch sphere, respectively, and interrogate the same LO. The joint interrogation allows to extend the inversion region for the unbiased estimation of a collective rotation angle θ from $[-\pi/2, \pi/2]$ (that is the case of a single Ramsey clock) to $[-\pi, \pi]$. This effectively extends the optimal Ramsey interrogation time (identified as the minimum of the Allan variance) and thus increases the absolute stability. We have demonstrated an improvement in the long-term stability of a factor of 2 for $1/f$ (flicker) noise and of a factor of 4 for white noise. The joint interrogation method is reminiscent of a protocol first introduced in the context of quantum phase estimation with single qubits [59] and also explored experimentally in gravity gradiometry with two atomic clouds [60]. The idea is here extended to coherent spin states of a large number of qubits and adapted to the context of atomic clocks.

It is important to clarify the significance of the figure of merit considered in this work. We have calculated the Allan variance of the stochastic variable Eq. (16), given by the difference between the true value of the accumulated phase and the estimated one at each Ramsey interrogation. Furthermore, the interrogation is stopped when the true value of the phase shift a properly defined inversion region. Experimentally, the true value of the phase is inaccessible. The significance of our study is to give a "safe" maximum Ramsey time where phase slips are negligible. Our paper thus shows that this safe maximum interrogation time can be extended when using the joint interrogation method. Finally, we have shown how the joint protocol can be combined with a recent proposal using spin-squeezed states to obtain a scaling of the stability faster than the SQL $\sigma^2_{\rm SQL} = O(1/N_t)$. Our proposal can be readily realized in state-of-the-art experimental implementations and addresses one of the major problems for current atomic clocks.

ACKNOWLEDGMENTS

We thank A. Bertolldi, K. Hammerer, F. Levi, M. Schulte, and M. Tarallo for discussions. We acknowledge funding of the project EMPIR-USOQS, EMPIR projects are cofunded by the European Unions Horizon2020 research and innovation program and the EMPIR Participating States. We also acknowledge support by the H2020 QuantERA ERA-NET cofund QCLOCKS. This research was supported by the National Key R&D Program of China (Grant No. 2017YFA0304500), National Natural Science Foundation of China (Grant No. 11874247), 111 project (Grant No. D18001), the Hundred Talent Program of the Shanxi Province (2018).

APPENDIX

We give here details on the numerical simulations performed in this paper. We numerically generate the correlated-noise LO signal following the discrete incremental method outlined in Ref. [61]. In Fig. 11 we show results of numerical simulations of the flicker noise generated numerically. The numerical code generates a vector $\delta\tilde{\omega}_{\rm LO}(t)/\omega_0$ at discrete times. In Fig. 11(a) we show the phase variance $v_1(t)^2 = \mathcal{E}_{\tilde{\omega}}[\tilde{\theta}_{\rm LO}(t)^2]$, where $\mathcal{E}_{\tilde{\omega}}$ indicates statistical averaging over LO fluctuations (obtained from 10^4 numerical realizations, the vector size being $n = 10^3$) and $\tilde{\theta}(t) = \int_0^t d\tilde{t}\, \tilde{\omega}_{\rm LO}(\tilde{t})$. In Fig. 11(b) we plot the power spectral density $S(f) = \mathcal{E}_{\tilde{\omega}}[|\delta\tilde{\omega}_{\rm LO}(f)|^2]$, where $\delta\tilde{\omega}_{\rm LO}(f)$ is the Fourier transform of the noise signal $\delta\tilde{\omega}_{\rm LO}(t)$. The numerical results follows very well the expected behavior $v_1(t)^2 = (\gamma_{\rm LO}t)^2$ and $S(f) \sim 1/f$ except for short times and large frequencies where there are some deviations.

In Figs. 11(c) and 11(d) we show examples of $P_T(n_c)$ for flicker noise, obtained for $\gamma_{\rm LO}T = 0.3$ and $\gamma_{\rm LO}T = 0.45$, respectively. Here and in the numerics shown in the main text, $P_T(n_c)$ are calculated from 5×10^4 noise realizations.

In the numerical simulations of the clock protocols the time step of the numerical noise generation is set equal to the Ramsey time T. In the simulations including dead time, the time step is set to T_D and T is taken as a multiple of T_D. Measurement results are generated numerically using $P(\mu|\theta) = |\langle\mu|\hat{U}(\theta)|\psi\rangle|^2$, depending on the interferometer input $|\psi\rangle$ and transformation $\hat{U}(\theta)$. For the large number of particles N, $P(\mu|\theta)$ is replaced by a Gaussian distribution centered at $\langle\hat{J}_z(\theta)\rangle_{\rm out}$ and of width $(\Delta\hat{J}_z(\theta))^2_{\rm out}$: the two approaches give the same results for small N. Statistical averaging in all plots shown in this paper is typically obtained for 2×10^4 realizations.

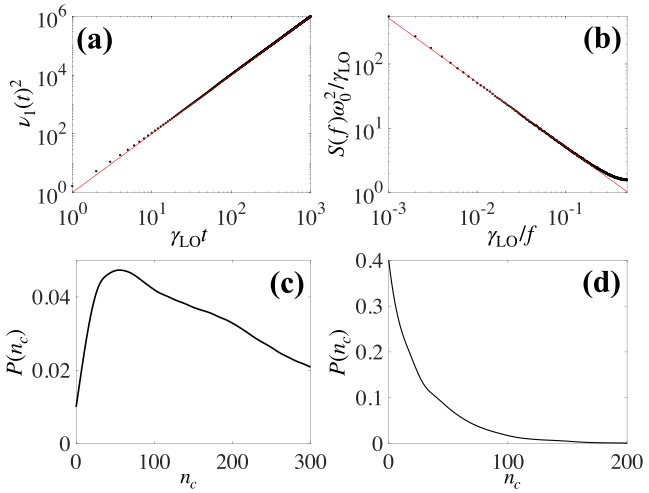

FIG. 11. (a) Phase variance as a function of $\gamma_{\rm LO}t$ (dots). The solid line is $v_1(t)^2 = (\gamma_{\rm LO}t)^2$. (b) Power spectral density as a function of $\gamma_{\rm LO}t$ (dots). The solid line is a fit $S(f) = h_{\rm LO}/f$ giving $h_{\rm LO} = 1/(2\chi\log 2) \times (\gamma_{\rm LO}/\omega_0)^2$ with $\chi = 1.4$. Panels (c) and (d) show $P_T(n_c)$ for $\gamma_{\rm LO}T = 0.3$ and $\gamma_{\rm LO}T = 0.45$, respectively.

[1] J. Vanier and C. Audoin, *The Quantum Physics of Atomic Frequency Standards* (Adam Higler, New York, 1992).

[2] R. Wynands, Atomic Clocks, Lect. Notes Phys. **789**, 363 (2009).

[3] F. Riehle, *Frequency Standards: Basics and Applications* (Wiley-VCH, Weinheim, Germany, 2004).

[4] N. Poli, C. W. Oates, P. Gill, and G. M. Tino, Optical atomic clocks, La Rivista del Nuovo Cimento **36**, 555 (2013).

[5] A. D. Ludlow, M. M. Boyd, J. Ye, E. Peik, and P. O. Schmidt, Optical atomic clocks, Rev. Mod. Phys. **87**, 637 (2015).

[6] N. F. Ramsey, *Molecular Beams* (Oxford University Press, New York, 1956).

[7] M. Takamoto, F.-L. Hong, R. Higashi, and H. Katori, An optical lattice clock, Nature (London) **435**, 321 (2005).

[8] Y. Y. Jiang, A. D. Ludlow, N. D. Lemke, R. W. Fox, J. A. Sherman, L. S. Ma, and C. W. Oates, Making optical atomic clocks more stable with 10^{-16} level laser stabilization, Nat. Photonics **5**, 158 (2011).

[9] M. J. Thorpe, L. Rippe, T. M. Fortier, M. S. Kirchner, and T. Rosenband, Frequency stabilization to 6×10^{-16} via spectral-hole burning, Nat. Photonics **5**, 688 (2011).

[10] T. Kessler, C. Hagemann, C. Grebing, T. Legero, U. Sterr, F. Riehle, M. J. Martin, L. Chen, and J. Ye, A sub-40-mhz-linewidth laser based on a silicon single-crystal optical cavity, Nat. Photonics **6**, 687 (2012).

[11] G. D. Cole, W. Zhang, M. J. Martin, J. Ye, and M. Aspelmeyer, Tenfold reduction of brownian noise in high-reflectivity optical coatings, Nat. Photonics **7**, 644 (2013).

[12] B. J. Bloom, T. L. Nicholson, J. R. Williams, S. L. Campbell, M. Bishof, X. Zhang, W. Zhang, S. L. Bromley, and J. Ye, An optical lattice clock with accuracy and stability at the 10^{-18} level, Nature (London) **506**, 71 (2014).

[13] N. Nemitz, T. Ohkubo, M. Takamoto, I. Ushijima, M. Das, N. Ohmae, and H. Katori, Frequency ratio of yb and sr clocks with 5×10^{-17} uncertainty at 150 seconds averaging time, Nat. Photonics **10**, 258 (2016).

[14] W. F. McGrew, X. Zhang, R. J. Fasano, S. A. Schäffer, K. Beloy, D. Nicolodi, R. C. Brown, N. Hinkley, G. Milani, M. Schioppo, T. H. Yoon, and A. D. Ludlow, Atomic clock performance enabling geodesy below the centimetre level, Nature (London) **564**, 87 (2018).

[15] V. Bužek, R. Derka, and S. Massar, Optimal Quantum Clocks, Phys. Rev. Lett. **82**, 2207 (1999).

[16] T. Rosenband and D. R. Leibrandt, Exponential scaling of clock stability with atom number, arXiv:1303.6357.

[17] D. B. Hume and D. R. Leibrandt, Probing beyond the laser coherence time in optical clock comparisons, Phys. Rev. A **93**, 032138 (2016).

[18] J. Borregaard and A. S. Sørensen, Efficient Atomic Clocks Operated with Several Atomic Ensembles, Phys. Rev. Lett. **111**, 090802 (2013).

[19] N. Shiga and M. Takeuchi, Locking the local oscillator phase to the atomic phase via weak measurement, New J. Phys. **14**, 023034 (2012).

[20] N. Shiga, M. Mizuno, K. Kido, P. Phoonthong, and K. Okada, Accelerating the averaging rate of atomic ensemble clock stability using atomic phase lock, New J. Phys. **16**, 073029 (2014).

[21] R. Kohlhaas, A. Bertoldi, E. Cantin, A. Aspect, A. Landragin, and P. Bouyer, Phase Locking a Clock Oscillator to a Coherent Atomic Ensemble, Phys. Rev. X **5**, 021011 (2015).

[22] A. Shankar, G. P. Greve, B. Wu, J. K. Thompson, and M. Holland, Continuous Real-Time Tracking of a Quantum Phase Below the Standard Quantum Limit, Phys. Rev. Lett. **122**, 233602 (2019).

[23] W. Bowden, A. Vianello, I. R. Hill, M. Schioppo, and R. Hobson, Improving the Q Factor of an Optical Atomic Clock Using Quantum Nondemolition Measurement, Phys. Rev. X **10**, 041052 (2020).

[24] G. Colangelo, F. M. Ciurana, L. C. Bianchet, R. J. Sewell, and M. W. Mitchell, Simultaneous tracking of spin angle and amplitude beyond classical limits, Nature (London) **543**, 525 (2017).

[25] R. Kaubruegger, D. V. Vasilyev, M. Schulte, K. Hammerer, and P. Zoller, Quantum Variational Optimization of Ramsey Interferometry and Atomic Clocks, Phys. Rev. X **11**, 041045 (2021).

[26] L. Pezzè and A. Smerzi, Heisenberg-Limited Noisy Atomic Clock Using a Hybrid Coherent and Squeezed State Protocol, Phys. Rev. Lett. **125**, 210503 (2020).

[27] L. Pezzè, A. Smerzi, M. K. Oberthaler, R. Schmied, and P. Treutlein, Quantum metrology with nonclassical states of atomic ensembles, Rev. Mod. Phys. **90**, 035005 (2018).

[28] F. T. Arecchi, E. Courtens, R. Gilmore, and H. Thomas, Atomic Coherent States in Quantum Optics, Phys. Rev. A **6**, 2211 (1972).

[29] Unless when necessary, we drop here the suffix A and AB to indicate the estimate obtained from the single and joint Ramsey interferometers, respectively. We also indicate with μ the result of a measurement, which is a single value for the single Ramsey interferometer or a double value in the case of the joint interferometer.

[30] D. W. Allan, Statistics of atomic frequency standards, Proc. IEEE **54**, 221 (1966).

[31] H. Cramèr, *Mathematical Methods of Statistics* (Princeton University Press, Princeton, NJ, 1946).

[32] C. R. Rao, Information and the accuracy attainable in the estimation of statistical parameters, Bull. Calcutta Math. Soc. **37**, 81 (1945).

[33] C. W. Helstrom, *Quantum Detection and Estimation Theory* (Academic, New York, 1976).

[34] S. L. Braunstein and C. M. Caves, Statistical distance and the geometry of quantum states, Phys. Rev. Lett. **72**, 3439 (1994).

[35] L. Pezzè and A. Smerzi, Quantum theory of phase estimation, in *Atom Interferometry, Proceedings of the International School of Physics Enrico Fermi, Course 188*, Varenna, edited by G. M. Tino and M. A. Kasevich, (IOS Press, Amsterdam, 2014), p. 691.

[36] It should be noticed that, if no phase slip occurs, the quantity y_n is typically small, of the order of $1/\sqrt{N}$. Instead, if one or more phase slips that occur up to the nth Ramsey cycles, then the quantity y_n is typically much larger than $1/\sqrt{N}$. Relatively rare slip events thus dominate the calculation of the Allan variance making it statistically unstable.

[37] W. M. Itano, J. C. Bergquist, J. J. Bollinger, J. M. Gilligan, D. J. Heinzen, F. L. Moore, M. G. Raizen, and D. J. Wineland, Quantum projection noise: Population fluctuations in two-level systems, Phys. Rev. A **47**, 3554 (1993).

[38] G. Santarelli, Ph. Laurent, P. Lemonde, A. Clairon, A. G. Mann, S. Chang, A. N. Luiten, and C. Salomon, Quantum Projection

Noise in an Atomic Fountain: A High Stability Cesium Frequency Standard, Phys. Rev. Lett. **82**, 4619 (1999)

[39] S. Bize, Y. Sortais, P. Lemonde, S. Zhang, P. Laurent, G. Santarelli, C. Salomon, and A. Clairon, Interrogation oscillator noise rejection in the comparison of atomic fountains, IEEE Trans. Ultrason. Ferroelectr. Freq. Control **47**, 1253 (2000).

[40] M. Takamoto, T. Takano, and H. Katori, Frequency comparison of optical lattice clocks beyond the Dick limit, Nat. Photonics **5**, 288 (2011).

[41] G. W. Biedermann, K. Takase, X. Wu, L. Deslauriers, S. Roy, and M. A. Kasevich, Zero-Dead-Time Operation of Interleaved Atomic Clocks, Phys. Rev. Lett. **111**, 170802 (2013).

[42] M. Meunier, I. Dutta, R. Geiger, C. Guerlin, C. L. Garrido Alzar, and A. Landragin, Stability enhancement by joint phase measurements in a single cold atomic fountain, Phys. Rev. A **90**, 063633 (2014).

[43] M. Schioppo, R. C. Brown, W. F. McGrew, N. Hinkley, R. J. Fasano, K. Beloy, T. H. Yoon, G. Milani, D. Nicolodi, J. A. Sherman, N. B. Phillips, C. W. Oates, and A. D. Ludlow, Ultrastable optical clock with two cold-atom ensembles, Nat. Photonics **11**, 48 (2017).

[44] G. J. Dick, Local oscillator induced instabilities in trapped ion frequency standards, in *Proceedings of the Precise Time and Time Interval Meeting*, US Naval Observatory (ION, Manassas, VA, 1987), pp. 133–147.

[45] C. Audoin, G. Santarelli, A. Makdissi, and A. Clairon, Properties of an oscillator slaved to a periodically interrogated atomic resonator, IEEE Trans. Ultrason. Ferroelectr. Freq. Control **45**, 877 (1998).

[46] A. Quessada, R. P. Kovacich, I. Courtillot, A. Clairon, G. Santarelli, and P. Lemonde, The Dick effect for an optical frequency standard, J. Opt. B: Quantum Semiclassical Opt. **5**, S150 (2003).

[47] G. Santarelli, C. Audoin, A. Makdissi, P. Laurent, G. J. Dick, and A. Clairon, Frequency stability degradation of an oscillator slaved to a periodically interrogated atomic resonator, IEEE Trans. Ultrason. Ferroelectr. Freq. Control **45**, 887 (1998).

[48] P. G. Westergaard, J. Lodewyck, and P. Lemonde, Minimizing the dick effect in an optical lattice clock, IEEE Trans. Ultrason., Ferroelect., Freq. Contr. **57**, 623 (2010).

[49] M. Schulte, C. Lisdat, P. O. Schmidt, U. Sterr, and K. Hammerer, Prospects and challenges for squeezing-enhanced optical atomic clocks, Nat. Commun. **11**, 5955 (2020).

[50] L. Pezzè and A. Smerzi, Quantum Phase Estimation Algorithm with Gaussian Spin States, PRX Quantum **2**, 040301 (2021).

[51] D. J. Wineland, J. J. Bollinger, W. M. Itano, and D. J. Heinzen, Squeezed atomic states and projection noise in spectroscopy, Phys. Rev. A **50**, 67 (1994).

[52] A. Louchet-Chauvet, J. Appel, J. J. Renema, D. Oblak, N. Kjaergaard, and E. S. Polzik, Entanglement-assisted atomic clock beyond the projection noise limit, New J. Phys. **12**, 065032 (2010).

[53] I. Kruse, K. Lange, J. Peise, B. Lücke, 1 L. Pezzè, J. Arlt, W. Ertmer, C. Lisdat, L. Santos, A. Smerzi, and C. Klempt, Improvement of an Atomic Clock using Squeezed Vacuum, Phys. Rev. Lett. **117**, 143004 (2016).

[54] O. Hosten, N. J. Engelsen, R. Krishnakumar, and M. A. Kasevich, Measurement noise 100 times lower than the quantum-projection limit using entangled atoms, Nature (London) **529**, 505 (2016).

[55] E. Pedrozo-Peñafiel, S. Colombo, C. Shu, A. F. Adiyatullin, Z. Li, E. Mendez, B. Braverman, A. Kawasaki, D. Akamatsu, Y. Xiao, and V. Vuletić, Entanglement on an optical atomic-clock transition, Nature (London) **588**, 414 (2020).

[56] A. André, A. S. Sørense, and M. D. Lukin, Stability of Atomic Clocks Based on Entangled Atoms, Phys. Rev. Lett. **92**, 230801 (2004).

[57] J. Borregaard and A. S. Sørensen, Near-Heisenberg-Limited Atomic Clocks in the Presence of Decoherence, Phys. Rev. Lett. **111**, 090801 (2013),

[58] B. Braverman, A. Kawasaki, and V. Vuletić, Impact of non-unitary spin squeezing on atomic clock performance, New J. Phys. **20**, 103019 (2018).

[59] A. Yu. Kitaev, A. Shen, and M. Vyalyi, *Classical and Quantum Computation* (American Mathematical Society, Providence, RI, 2002).

[60] F. Sorrentino *et al.*, Simultaneous measurement of gravity acceleration and gravity gradient with an atom interferometer, Appl. Phys. Lett. **101**, 114106 (2012).

[61] J. Kasdin, Discrete simulation of colored noise and stochastic processes and $1/f^{a}$ power law noise generation, Proc. IEEE **83**, 802 (1995).